
BAYESIAN HIERARCHICAL MODELS FOR QUANTITATIVE ESTIMATES FOR PERFORMANCE METRICS APPLIED TO SADDLE SEARCH ALGORITHMS

A PREPRINT

 **Rohit Goswami***

Science Institute and Faculty of Physical Sciences
University of Iceland, 107 Reykjavík, Iceland

Also at: Department of Mechanical and Materials Engineering
Queen’s University, 60 Union Street, Kingston, Ontario, Canada

rgoswami@ieee.org

July 24, 2025

ABSTRACT

Rigorous performance evaluation is essential for developing robust algorithms for high-throughput computational chemistry. Traditional benchmarking, however, often struggles to account for system-specific variability, making it difficult to form actionable conclusions. We present a Bayesian hierarchical modeling framework that rigorously quantifies performance metrics and their uncertainty, enabling a nuanced comparison of algorithmic strategies. We apply this framework to analyze the Dimer method, comparing Conjugate Gradient (CG) and L-BFGS rotation optimizers, with and without the removal of external rotations, across a benchmark of 500 molecular systems. Our analysis confirms that CG offers higher overall robustness than L-BFGS in this context. While the theoretically-motivated removal of external rotations led to higher computational cost (~40% more energy and force calls) for most systems in this set, our models also reveal a subtle interplay, hinting that this feature may improve the reliability of the L-BFGS optimizer. Rather than identifying a single superior method, our findings support the design of adaptive “chain of methods” workflows. This work showcases how a robust statistical paradigm can move beyond simple performance rankings to inform the intelligent, context-dependent application of computational chemistry methods.

Keywords Bayesian statistics, performance measures

1 Introduction

Locating transition states (TS), first-order saddle points on potential energy surfaces (PES), is fundamental to understanding reaction mechanisms and kinetics in chemistry [10, 42]. Numerous algorithms target this challenge, with minimum mode following (MMF) methods forming a prominent class [7]. These algorithms, initiated from a single point on the PES, iteratively ascend the minimum curvature mode while relaxing orthogonal directions. Notable MMF families include Lanczos-based Activation Relaxation Technique Nouveau (ARTn) methods [5, 19, 35, 36, 43] and the two-point Dimer method [20], which uses a pair of images to estimate the minimum mode direction. This is in turn an independent implementation of the hybrid eigenvector-following algorithm [37]. Other variations employ internal coordinates [21] or iteratively build PES approximations [16, 27].

Evaluating and comparing such algorithms typically relies on benchmarks, from established sets like Baker’s [2] to more recent collections [8]. However, studies introducing methodological advancements often demonstrate performance on limited sets of small systems, frequently using computationally inexpensive potentials [26, 27, 30, 33, 41, 48]. This

*Corresponding Author

traditional benchmarking paradigm appears increasingly misaligned with current computational practice, where peta- and exa-scale resources combined with workflow engines [24, 34] enable large-scale, systematic explorations across diverse chemical spaces. Simple performance comparisons based on small benchmarks or average metrics often neglect significant system-to-system variability and potential implementation biases [11, 28], providing an inadequate basis for selecting optimal methods for demanding high-throughput applications.

To bridge this gap, we advocate for and demonstrate a rigorous statistical framework using Bayesian generalized linear mixed-effects models (GLMMs) for analyzing algorithm performance data from large benchmark sets. This approach, implemented via the `brms` R package [4] interfacing with Stan [6], robustly handles the statistical modeling of various performance metrics (e.g., computation time, PES call counts, binary success) and explicitly models the hierarchical structure of benchmark data (e.g., multiple runs within chemical systems) using random effects. Crucially, the Bayesian paradigm provides comprehensive uncertainty quantification through full posterior distributions and credible intervals, facilitating nuanced and reliable comparisons beyond simple point estimates or visual inspection.

In this work, we apply this Bayesian GLMM framework to analyze the performance trade-offs associated with two common variations within the Dimer method: the choice between Conjugate Gradient (CG) and Limited-memory BFGS (L-BFGS) optimizers for the rotational step [26], and the effect of enabling or disabling the removal of external rotation and translation degrees of freedom [33]. We utilize the EON software package [9] interfaced with NWChem [1] at the HF/3-21G level of theory, analyzing performance across a diverse benchmark set of 500 initial configurations near saddle points introduced by Hermes et al. [21].

The remainder of this paper is structured as follows: Section 2 details the Dimer method variants and the statistical models employed. Section 3 presents the results of applying these models to the benchmark dataset. Section 4 discusses the implications of the findings and the advantages of the statistical approach, and Section 5 provides concluding remarks.

2 Methods

2.1 Dimer method

The Dimer method [20] is a single-ended saddle search method that algorithmically finds first-order saddle point geometries by iteratively refining the position R (a $3N$ -dimensional vector representing the system coordinates) and orientation \hat{N} (a unit vector in $3N$ dimensions) of a ‘‘dimer’’. An alternative formulation of the same was demonstrated earlier via the hybrid-eigenvector following using the variational Rayleigh-Ritz to find the eigenvalue and eigenvector pair [37]. The dimer consists of two system images, R_1 and R_2 , separated by a small fixed distance ΔR along the dimer axis \hat{N} :

$$R_1 = R - \frac{\Delta R}{2} \hat{N} \quad (1)$$

$$R_2 = R + \frac{\Delta R}{2} \hat{N} \quad (2)$$

The core idea is to rotate the dimer orientation \hat{N} to align with the lowest curvature mode at the midpoint R , and then translate R uphill along this mode (if curvature is negative) while minimizing energy in all other directions. This process typically involves two main steps per iteration: rotation and translation.

The goal of the rotation step is to find the orientation \hat{N} that minimizes the dimer’s energy, keeping the midpoint R fixed. This corresponds to aligning \hat{N} with the direction of lowest local curvature. The rotational dynamics are driven by the component of the sum of forces at the endpoints perpendicular to the dimer axis, $F_{rot} = (F_1 + F_2) - ((F_1 + F_2) \cdot \hat{N}) \hat{N}$, where $F_1 = F(R_1)$ and $F_2 = F(R_2)$. The rotation aims to drive F_{rot} to zero.

Calculating the exact energy curvature requires the Hessian matrix. To avoid this computational expense, the Dimer method typically employs approximations based only on energies and forces at the endpoints R_1 and R_2 . Following the approach refined by Olsen et al. [41], the curvature along the dimer axis $C(\hat{N})$ and an effective torque or rotational force $\tau(\hat{N})$ can be estimated efficiently and iteratively until a threshold for the rotational force is reached. The finite difference approximation for the curvature is:

$$C(\hat{N}) \approx \frac{(F_2 - F_1) \cdot \hat{N}}{\Delta R} \quad (3)$$

The rotational force $\tau(\hat{N})$, which is perpendicular to \hat{N} , can also be estimated from F_1 and F_2 [22]. An optimization algorithm, such as Conjugate Gradient (CG) or Limited-memory BFGS (L-BFGS) as investigated in this work, is then

used to iteratively update the orientation \hat{N} (typically by small rotations) to minimize the energy with respect to rotation, effectively driving $\tau(\hat{N})$ towards zero.

Once the dimer is aligned with the estimated lowest mode direction \hat{N} , the midpoint R is moved towards the saddle point. The translation is guided by an effective force F_{trans} . If the estimated curvature $C(\hat{N})$ is negative (indicating an uphill direction towards the saddle), the force component parallel to \hat{N} is inverted. The effective force for the optimizer is:

$$F_{trans}(R) = F(R) - 2(F(R) \cdot \hat{N})\hat{N} \quad \text{if } C(\hat{N}) < 0 \quad (4)$$

If $C(\hat{N}) \geq 0$, the unmodified force $F(R)$ might be used, or other strategies employed to ensure movement towards a saddle point. A standard optimization algorithm (often L-BFGS in many implementations) then takes a step using this effective force to update the midpoint:

$$R_{k+1} = \text{OptimizerStep}(R_k, F_{trans}(R_k)) \quad (5)$$

The rotation and translation steps are repeated iteratively until convergence criteria, typically based on the magnitude of the total force $F(R)$, are met.

2.2 Statistical models

Quantitative assessment of saddle point search algorithm performance requires rigorous statistical methods, particularly when comparing multiple algorithms across diverse chemical systems. While foundational studies have provided crucial insights [2, 21, 26, 27], analyses often rely on qualitative comparisons or the eyeball norm and summary statistics based on relatively small datasets. Such approaches may not fully capture performance variability or allow for robust statistical inference regarding the significance and magnitude of performance differences. When larger system sets are used they are often hampered by point-estimates of error like the root mean square deviation [12, 45]. It is important to note that much of the saddle search literature for molecular systems makes several approximations valid for small angles or well behaved portions of the energy landscape, which may not hold in practice.

The number of potential energy surface (PES) calls (computational cost) represents count data, total computation time is typically positive and right-skewed, and search success is a binary outcome. These data types often violate the assumptions inherent in standard linear models (e.g., normality, homoscedasticity) [40]. Additionally, comparing algorithm performance typically involves applying multiple methods to the same set of chemical systems, resulting in repeated measures or clustered data. Observations from the same system are not independent, and failing to account for this structure can lead to inaccurate standard errors and potentially flawed conclusions. Variability arising from different software implementations or environments can also present challenges [28], underscoring the need for reproducible analyses.

To analyze the saddle search results, we focus on interpreting three algorithmic concerns, the computational cost, the total time taken, and the success ratio. These are considered in the context of varying the optimizer used in the rotation phase (CG versus LBFS) and the effect of using rotation removal (yes versus no) thus forming 4 sets of measurements on the 500 systems. We employed Bayesian generalized linear mixed-effects models [31]. This framework is well-suited to the data structure and research questions. GLMMs explicitly model the appropriate response distribution for each outcome (counts, continuous time, binary success) using link functions, while incorporating random effects to account for the repeated measures structure (i.e., baseline differences between systems). The Bayesian approach provides full posterior distributions for parameter estimates, facilitating comprehensive uncertainty quantification via credible intervals and enabling principled model comparison [4]. We use brms [4] to construct a Stan model [6] which is compiled into C++ code for analysis with the no U turn sampler (NUTS) [23]. These models are so efficient that they are run on a local machine with CPU configuration of 13th Gen Intel i7-1365U (12) @ 5.200GHz with 30 GB of available memory. Details of model fitting, prior specification, and convergence diagnostics are provided in the Supplementary Information.

2.2.1 Effect structures considered

All statistical models employed shared a common approach to constructing the linear predictor, denoted by η_{ij} , which corresponds to observation i on system j . The expected value of the outcome (μ_{ij}) is related to this linear predictor via an appropriate link function $g(\cdot)$, i.e., $g(\mu_{ij}) = \eta_{ij}$, with the specific link function and response distribution detailed below for each outcome type.

Each linear predictor η_{ij} included a random intercepts u_j , to account for the repeated measures within system j , i.e. $u_j \sim \text{Normal}(0, \sigma_u^2)$.

The fixed-effects component was varied systematically to address different analytical questions. The specific fixed-effects structures examined were:

$$\text{Fixed Effects}_{ij} = \begin{cases} \beta_0 + \beta_1 \text{DR}_{i(j)} & (\text{RotOptimizer}) \\ \beta_0 + \beta_2 \text{RR}_{i(j)} & (\text{RotRemoval}) \\ \beta_0 + \beta_1 \text{DR}_{i(j)} + \beta_2 \text{RR}_{i(j)} \\ \quad + \beta_3 (\text{DR}_{i(j)} \times \text{RR}_{i(j)}) & (\text{Full}) \end{cases} \quad (6)$$

Here, β_k represents fixed-effects coefficients (intercept and slopes), $\text{DR}_{i(j)}$ is an indicator variable for the dimer rotation optimizer used (CG or L-BFGS) for observation i within system j , and $\text{RR}_{i(j)}$ is an indicator variable for rotation removal ('no' or 'yes') within system j . The $\text{DR}_{i(j)} \times \text{RR}_{i(j)}$ term represents their interaction.

The first two effect settings focus on the main effect of a single factor (RotOptimizer or RotRemoval, respectively). When fitted to the complete dataset, these estimate the effect of the included factor while marginalizing over the levels of the excluded factor. Alternatively, as detailed in the Results for specific targeted comparisons, these structures might be applied to subsets of the data (e.g., comparing optimizers only when rotations are removed).

The third effect setting considers the main effects of the dimer rotation optimizer and the rotation removal. The fourth effect setting represents the full interaction model. It simultaneously estimates the main effects of both factors and their interaction term. This model generally utilizes data from all four conditions per system (where available) to provide the most comprehensive assessment of how the factors jointly influence the outcome.

This approach allows for both focused investigation of individual factor effects, potentially mirroring simpler experimental designs, and a detailed analysis of their interplay using the full statistical power of the dataset within the multilevel framework. The specific response distribution and link function for each outcome metric are detailed in the following sections.

2.2.2 Modeling algorithmic efficiency

The primary figure of merit for saddle search algorithms, particularly when introducing new methodologies, is the number of calls made to the underlying potential energy surface (PES). This metric, referred throughout this manuscript as "PES calls," directly correlates with computational cost, especially when high-level electronic structure methods are employed.

PES calls represent count data [40], which typically violate the assumptions of standard linear models, which assume the response variable is normally distributed. Beyond this, the difficulty of applying frequentist measures of statistical significance like the p-value for applied situations is fraught with controversy [29, 32]. As demonstrated in the Supplementary Information, even linear mixed-effects models, which account for per-molecule variability, can produce misleading results when applied directly to count data without appropriate transformations or distributional assumptions.

For comparing PES calls, we employed Bayesian generalized linear mixed-effects models (GLMMs) with a negative binomial response distribution with a logarithmic link function, which has support on the non negative integers. This distribution is appropriate for overdispersed count data like PES calls [40]. We thus use:

$$\begin{aligned} \text{PESCalls}_{ij} &\sim \text{NegativeBinomial}(\mu_{ij}, \phi) \\ \log(\mu_{ij}) &= \text{Fixed Effects}_{ij} + u_j \end{aligned} \quad (7)$$

where PESCalls_{ij} represents the observed PES calls for the i^{th} observation on system j ; μ_{ij} is the expected value; ϕ is the shape parameter of the negative binomial distribution; Fixed effects Eq. 12 comprise of the overall intercept and effect of the method; and u_j is a random intercept for chemical system j , accounting for the paired nature of the data and modeled as $u_j \sim \text{Normal}(0, \sigma_u^2)$.

2.2.3 Modeling total time

Total time analysis for saddle search algorithms is often perilous, since the bulk of compute intensive calculation are offloaded to external codes like VASP, ORCA etc. which may have strong scaling and depend heavily on the specific functional form of the energy function along with the runtime environment. Additionally, compared to the cost of making PES calls, the time spent within the saddle search algorithm is almost always negligible. Nevertheless, since total wall time elapsed is of practical importance, it provides a valid algorithmic constraint for decision making.

For estimating the effect on total computation time, a similar GLMM structure was employed. Given that time is a continuous, positive, and often right-skewed variable, we used a Gamma response distribution with a logarithmic link function:

$$\begin{aligned} \text{TotalTime}_{ij} &\sim \text{Gamma}(\mu_{ij}, \alpha) \\ \log(\mu_{ij}) &= \text{Fixed Effects}_{ij} + u_j \end{aligned} \tag{8}$$

where TotalTime_{ij} is the computation time for observation i on system j , μ_{ij} is the expected time, α is the shape parameter of the Gamma distribution (inversely related to the variance when the variance is presented in terms of the squared mean). The linear predictor $\log(\mu_{ij})$ incorporates the fixed effects specified in Eq. 12 and the system-specific random intercept u_j , which is modeled as $u_j \sim \text{Normal}(0, \sigma_u^2)$.

2.2.4 Modeling success probabilities

To analyze the factors influencing the likelihood of a successful saddle point search convergence, we fitted a Bayesian generalized linear mixed model appropriate for binary outcomes. This involved using a Bernoulli response distribution and a logit link function:

$$\begin{aligned} \text{Success}_{ij} &\sim \text{Bernoulli}(p_{ij}) \\ \text{logit}(p_{ij}) &= \log\left(\frac{p_{ij}}{1 - p_{ij}}\right) = \text{Fixed Effects}_{ij} + u_j \end{aligned} \tag{9}$$

Here, Success_{ij} is a binary indicator for observation i on system j , p_{ij} is the probability of success, $\text{logit}(p_{ij})$ is the log-odds of success, and the linear predictor incorporates the fixed effects specified in Eq. (12) and the system-specific random intercept u_j , which is modeled as $u_j \sim \text{Normal}(0, \sigma_u^2)$.

This model allows us to estimate how the different factors influence the odds of a successful search, while accounting for baseline differences in success rates across systems.

3 Applications

To demonstrate the utility of leveraging a Bayesian approach to performance statistics, we analyse the performance of the dimer method variants on the dataset of 500 initial configurations for small gas-phase organic molecules (7-25 atoms) introduced by (author?) [21]. Saddle point searches were conducted using the EON software package [9]², interfaced with NWChem [1] as the quantum mechanical engine. Energies and forces were calculated at the Hartree-Fock (HF) level of theory using RHF (restricted HF) for singlets and UHF (unrestricted HF) for doublets [25] with the 3-21G basis set. Saddle searches algorithms were considered converged when the maximum component of the atomic forces fell below 0.01 eV/Å. This rather loose tolerance was chosen to highlight the effect of rotation removal, as the step sizes decrease on approaching the saddle and are less likely to lead to spurious rotation. Additionally, tighter tolerances tend to put more focus on the parameters of the underlying computational engine which is not the primary goal here. Comprehensive details regarding computational parameters, including self-consistent field thresholds, specific EON settings, and interface configurations, are provided in the Supplementary Information.

All models involved pairwise comparisons of dimer control modalities, using data filtered to include only systems where both methods in the pair successfully converged, and with the same saddle, with an energy difference of less than 0.01eV. Full interaction models are also fit. Since both PES calls and total time are proxies for computational effort, only the PES calls are presented here, with the total time model in the Supplementary.

3.1 Data overview

We applied the four dimer method variants (combinations of CG/L-BFGS rotation optimizers and enabling/disabling rotation removal) to the benchmark set of 500 initial configurations. An initial exploratory analysis of the performance metrics provides context for the subsequent Bayesian modeling, focusing here on the number of potential energy surface (PES) calls for successful runs and overall convergence success.

Figures 1 and 2 illustrate the difference in PES calls required for convergence, comparing pairs of calculations that reached the same saddle point (within 0.01 eV). When rotation removal was disabled (Fig. 1, 440 comparable systems),

²Using the Github variant: <https://github.com/TheochemUI/eOn>

the CG-rotations dimer required fewer PES calls than L-BFGS-rotations in a majority of cases (55%, median reduction 21 calls), although L-BFGS is rather comparable in performance (in 43% cases, median reduction 16 calls). With CG-rotations (Fig. 2, 465 comparable systems), disabling rotation removal was markedly more efficient, requiring fewer PES calls than enabling it in over 99% of systems (median reduction 126 calls). Both figures indicate that performance differences tend to be larger for systems starting with higher initial RMSD values relative to the saddle point.

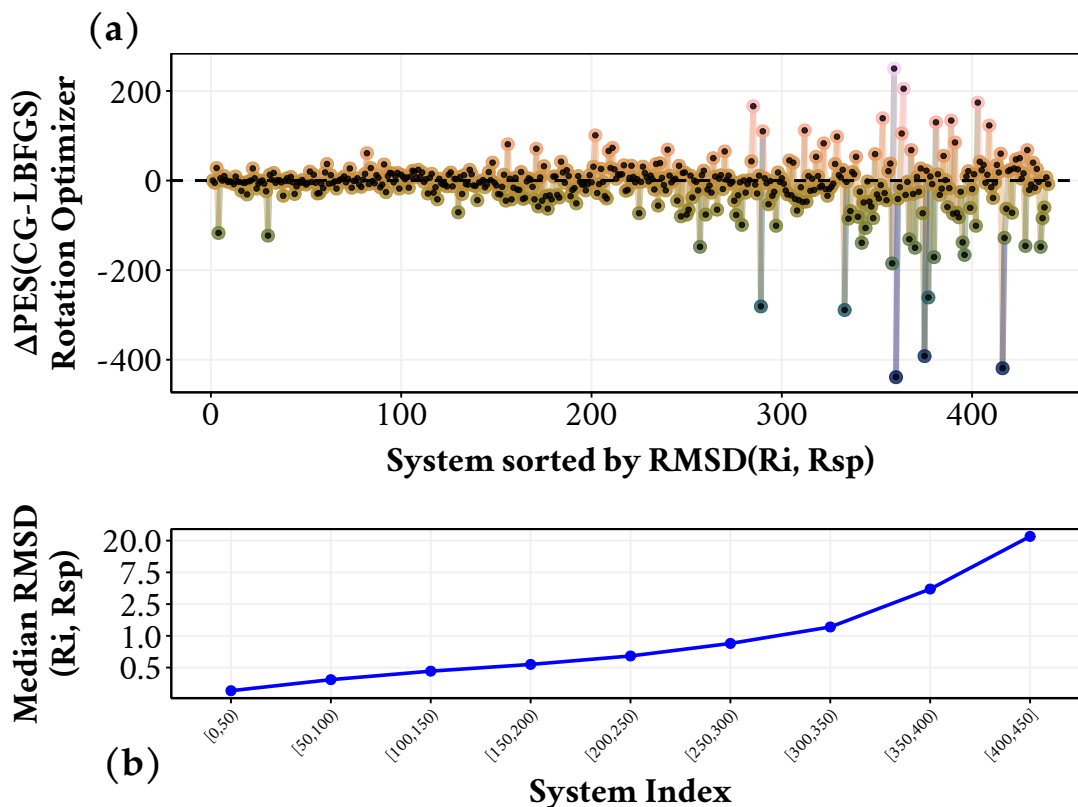


Figure 1: (a) Difference in the number of potential energy surface (PES) calls between L-BFGS and conjugate gradient (CG) rotations for dimer calculations that converged to the same saddle, defined as having a final energy difference of less than 0.01 eV. The x-axis represents the system index, sorted by the median RMSD. The y-axis displays the difference in PES calls, for changing the optimizer for the rotation of the dimer when rotation removal is not used. Consequently, negative values indicate that the CG algorithm required fewer PES calls (i.e., CG performed better), while positive values indicate that L-BFGS required fewer PES calls (i.e., LBFGS performed better). The median improvement is 21 calls occurring in 55.23% systems for CG-rotations compared to a median improvement of 16 calls in 43.18% systems for LBFGS-rotations across 440 systems. Systems which are farther away from the saddle point show a larger improvement with CG-rotations. (b) For the systems shown in (a), their log(median RMSD) plotted against System Index, with Median RMSD displayed on the y-axis.

Beyond the computational cost for successful runs, the overall convergence success is critical. Figure 3 presents a comparison of binary success outcomes across all 500 systems for which both methods in each comparison pair were run. High rates of joint success (where both compared methods converged) were generally observed across conditions. However, differences favouring the CG optimizer's robustness are apparent. When comparing optimizers directly, CG achieved unique success (succeeding when LBFGS failed) considerably more often than LBFGS did, both with rotation removal enabled (3.6% vs 0.6%, panel a) and disabled (5.8% vs 1.6%, panel b). Disabling rotation removal slightly reduced joint success rates and increased joint failures from 1.8% to 4.2% when comparing the optimizers. Examining the impact of rotation removal itself highlights CG's robustness further: using the CG optimizer (panel c), success rates remained very high (~96% joint success) with minimal sensitivity, as disabling rotation removal resulted in unique success in only 0.8% of cases. Conversely, using the LBFGS optimizer (panel d), disabling rotation removal significantly impacted performance; while joint success was still high (90.6%), unique successes for the enabled rotation removal setting were more frequent (4.0% vs 1.8% for disabled), and the joint failure rate rose notably to 3.6%. This

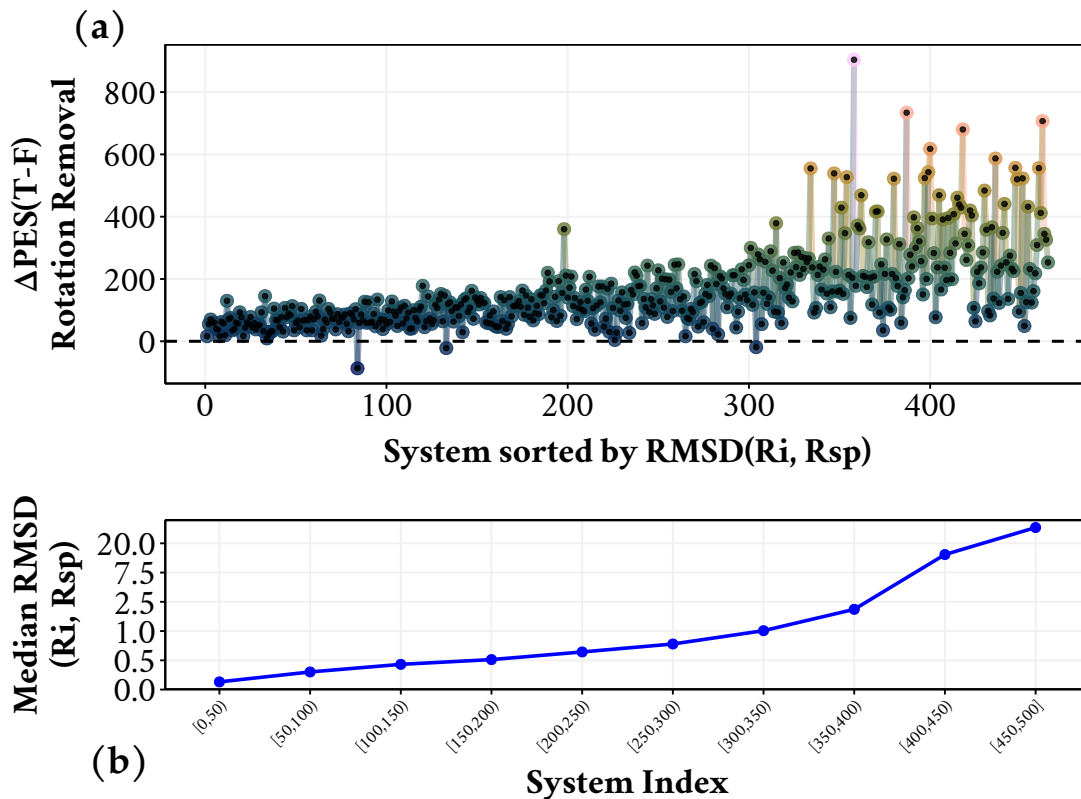


Figure 2: (a) Difference in the number of potential energy surface (PES) calls between using rotation removal (T) and not using rotation removal (F) for dimer calculations that converged to the same saddle, defined as having a final energy difference of less than 0.01 eV. The x-axis represents the system index, sorted by the median RMSD. The y-axis displays the difference in PES calls, using CG-rotations with and without rotation removal. Consequently, negative values indicate that the rotation removal required fewer PES calls (i.e., it performed better), while positive values indicate turning off the rotation removal took fewer PES calls (i.e., no rotation removal performed better). The median improvement is 126 calls occurring in 99.35% systems for rotation removal not being used compared to a median improvement of 22 calls in 0.65% systems when rotation removal is used across 465 systems. Systems which are farther away from the saddle point show a larger improvement without rotation removal. (b) For the systems shown in (a), their $\log(\text{median RMSD})$ plotted against System Index, with Median RMSD displayed on the y-axis.

suggests CG is less perturbed by the absence of rotation removal. As observed previously, convergence failures tend to concentrate at higher initial RMSD values, particularly in scenarios involving LBFGS without rotation removal.

This initial overview highlights apparent performance trends and differences between the method variants. However, these direct comparisons and visual inspections do not fully quantify the uncertainty associated with these effects or rigorously account for system-specific variability and potential interactions between the optimizer choice and rotation removal. Therefore, we employ the Bayesian hierarchical models detailed in Section 2.2 for a more robust statistical analysis of these metrics.

It is important to note that there are alternative methods for removing global rotations and translations, such as those implemented in OPTIM [47]. In OPTIM, the Rayleigh-Ritz procedure [37] and subsequent partial tangent space minimization involve orthogonalization to overall translation or rotation. However, the application demonstrated here follows the quaternion-based method implemented in EON [33].

3.2 Effort analysis model

To quantify the effects of the dimer rotation optimizer and rotation removal on computational effort, we analyzed the number of PES calls using the Bayesian negative binomial generalized linear mixed-effects model described in Section

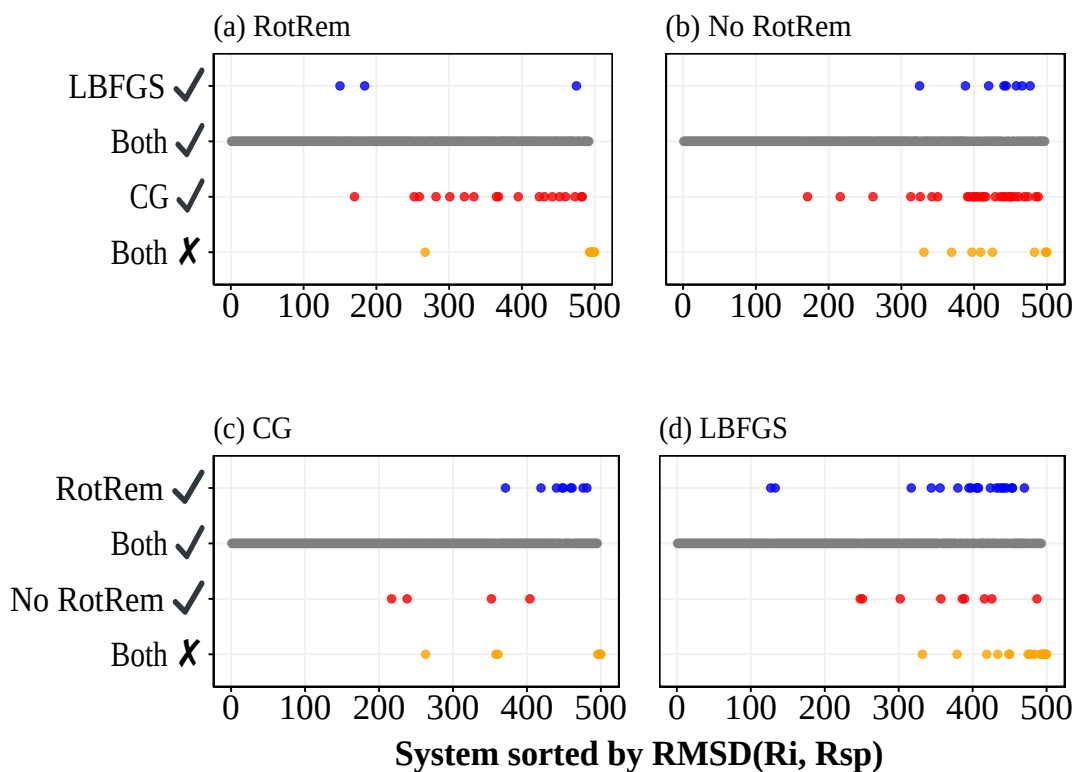


Figure 3: Binary convergence outcomes for dimer method calculations across 500 systems, ordered by median root-mean-squared-displacement (RMSD) of the initial geometry relative to the saddle point geometry. Each panel directly compares two settings, with the vertical position and color indicating the outcome. Gray points indicate where both compared settings succeed. Yellow points indicate where both compared settings fail. (a) Comparing LBFGS (blue) and CG (red) with rotation removal enabled, both methods (gray) succeeded in 94.0% of systems, while CG additionally succeeded (red) in 3.6% (LBFGS in 0.6%, blue) and both failed (yellow) in 1.8%. (b) Without rotation removal, comparing LBFGS (blue) to CG (red) yielded 90.8% joint success (gray), with 5.8% (red) unique CG successes (LBFGS in 1.6%, blue) while the joint failure is 4.2% (yellow). (c) Contrasting rotation removal (blue) with no rotation removal (red) using the CG-rotations shows high joint success (95.8%, gray) with 0.8% additional (red) without removal (1.8% with rotation removal, blue) and 1.6% cases where both fail (yellow). (d) For the LBFGS optimizer, comparing across rotation removal (blue) resulted in 90.6% joint success (gray), without rotation removal (red) 1.8% additional successes while with rotation removal (blue) 4% additional cases succeed, and there are 3.6% joint failures (yellow). Failures, particularly the unique failures with LBFGS without rotation removal, are concentrated at higher RMSD values.

2.2 (Eq. 7). We fitted models corresponding to the different fixed-effects structures defined in Eq. 12, examining main effects within relevant data subsets as well as the full interaction model using all comparable data.

$$\begin{aligned}
 \text{PESCalls}_{ij} &\sim \text{NegativeBinomial}(\mu_{ij}, \phi) \\
 \log(\mu_{ij}) &= \eta_{ij} \\
 \eta_{ij} &= \begin{cases} \beta_0 + \beta_1 \text{DR}_{i(j)} + u_j & \text{(a)} \\ \beta_0 + \beta_2 \text{RR}_{i(j)} + u_j & \text{(b)} \\ \beta_0 + \beta_1 \text{DR}_{i(j)} & \\ + \beta_2 \text{RR}_{i(j)} + \beta_3 (\text{DR}_{i(j)} \times \text{RR}_{i(j)}) + u_j & \text{(c)} \end{cases} \quad (10) \\
 u_j &\sim \text{Normal}(0, \sigma_u^2)
 \end{aligned}$$

First, applying the RotOptimizer model structure (Eq. (10)a), specifically to calculations where rotation removal was disabled, we examine the effect of the rotation optimizer (β_1). Switching from the CG reference to the L-BFGS optimizer resulted in a small but statistically credible increase in the median number of PES calls by 2.6% (95% CrI: [1.1%, 4.1%]). This suggests a slight efficiency advantage, in terms of PES calls, for the CG optimizer under these conditions.

Next, using the RotRemoval model structure (Eq. (10)b) applied to calculations using the CG optimizer, we examine the effect of enabling rotation removal (β_2). Enabling rotation removal led to a substantial and credible increase in the median PES calls by 41.5% (95% CrI: [38.6%, 44.4%]) compared to disabling it. This indicates a significant computational cost penalty associated with enabling rotation removal when using the CG optimizer in this setup.

Finally, the full interaction model (Eq. (10)c), incorporating both factors and their interaction simultaneously across 1805 valid observations, corroborated the main effects observed in the subset models (posterior distributions shown in Figure 4). The estimated median increase in PES calls for L-BFGS relative to CG (when rotation removal is off, β_1) was 2.6% (95% CrI: [0.7%, 4.5%]), corresponding to a multiplicative factor credibly just above 1 (median 1.03). Similarly, the median increase for enabling rotation removal relative to disabling it (when using CG, β_2) was substantial at 44.2% (95% CrI: [41.6%, 46.8%]), clearly visualized by the distribution centered around a multiplicative factor of 1.44 in Figure 4. The 95% credible interval for the interaction term (β_3), visually overlapping 1 in Figure 4 (multiplicative factor median 1.01, 95% CrI [0.99, 1.04]), provides no strong evidence that the effect of the optimizer choice significantly depends on the rotation removal setting, or vice versa. Furthermore, this full model estimated the standard deviation of the random intercepts for each system to be substantial (median $\sigma_u = 0.63$, 95% CrI: [0.59, 0.67] on the log scale), indicating significant system-specific variation in the baseline number of PES calls required for convergence, independent of the method variations.

These findings from the hierarchical models, which account for system variability via random intercepts ($\sigma_u \approx 0.63$), reinforce the trends observed in the exploratory data analysis (Fig. 1 and Fig. 3). They quantify the consistent, albeit small, PES call advantage of CG over L-BFGS (β_1) and the considerable computational overhead incurred by enabling this particular rotation removal implementation (β_2) for this dataset. The model diagnostics, including posterior predictive checks and residual analyses (shown for individual models in the preceding code sections, further details in SI), indicate reasonable model fit for the purpose of comparing these relative effects, despite some remaining heteroscedasticity common in complex chemical datasets.

3.3 Success rate model

We next analyzed the factors influencing the probability of successful convergence using the Bayesian Bernoulli generalized linear mixed-effects model specified in Section 2.2 (Eq. 11). Effects are reported as Odds Ratios (OR), representing the multiplicative change in the odds of success compared to a reference condition. An OR > 1 indicates increased odds, OR < 1 indicates decreased odds, and a 95% Credible Interval (CrI) that excludes 1 suggests a statistically credible effect.

$$\begin{aligned}
 \text{Success}_{ij} &\sim \text{Bernoulli}(p_{ij}) \\
 \text{logit}(p_{ij}) &= \log\left(\frac{p_{ij}}{1-p_{ij}}\right) = \eta_{ij} \\
 \eta_{ij} &= \begin{cases} \beta_0 + \beta_1 \text{DR}_i + u_j & \text{(a)} \\ \beta_0 + \beta_2 \text{RR}_i + u_j & \text{(b)} \\ \beta_0 + \beta_1 \text{DR}_i + \beta_2 \text{RR}_i + \beta_3 (\text{DR}_i \times \text{RR}_i) + u_j & \text{(c)} \end{cases} \quad (11) \\
 u_j &\sim \text{Normal}(0, \sigma_u^2)
 \end{aligned}$$

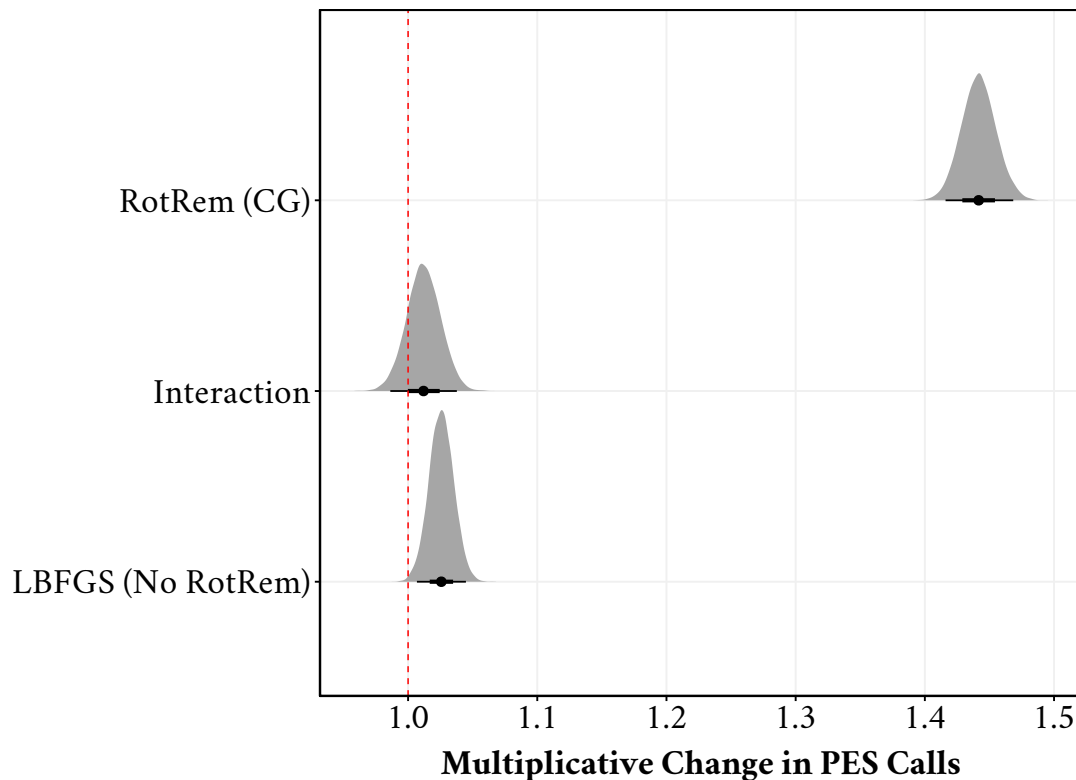


Figure 4: Posterior distributions of fixed effects on the multiplicative scale for PES calls from the full interaction model. The x-axis represents the factor by which expected PES calls change relative to the baseline (CG optimizer, rotation removal disabled), with the dashed line at $x=1$ indicating no effect. Distributions show the main effect of using L-BFGS (vs CG, when rotation removal is disabled), the main effect of enabling rotation removal (vs disabling, when using the CG optimizer), and their interaction. Thick lines represent 95% credible intervals with median dots. Enabling rotation removal shows a large multiplicative increase (~ 1.44), L-BFGS shows a small increase (~ 1.03), and the interaction credibly includes 1.

First, applying the RotOptimizer model structure (Eq. (11)a) specifically to the subset of calculations where rotation removal was disabled, we examined the effect of the optimizer (β_1). L-BFGS showed significantly lower odds of success compared to the CG reference. The estimated median OR for L-BFGS relative to CG was 0.3 (95% CrI: [0.13, 0.60]), indicating that the odds of convergence with L-BFGS were roughly only 30% of the odds with CG under these conditions. This model also revealed substantial variability between systems in their baseline odds of success (posterior median $s_u = 2.6$ on the log-odds scale, 95% CrI: [1.67, 3.81]).

Next, using the RotRemoval model structure (Eq. (11)b) specifically to the subset of calculations using CG-rotations, we examined the effect of rotation removal (β_2). The median OR for enabling rotation removal versus disabling it was 2.0 (95% CrI: [0.73, 6.35]). Although the point estimate suggests doubled odds of success when enabling rotation removal, the wide credible interval comfortably includes 1. Consequently, this model provides no strong statistical evidence that enabling rotation removal significantly alters the odds of success compared to disabling it when using the CG optimizer. Substantial between-system variability in baseline success odds was again noted (median $\text{sd}(\text{Intercept}) = 4.2$, 95% CrI: [2.63, 6.91] from this model's summary; the full model estimate is used below for consistency).

Finally, the full interaction model (Eq. (11)c), analyzing all 2000 observations across the four conditions, allowed for a detailed assessment of success odds. While the predicted probability of success for an average system is very high (~ 0.98) under all conditions, as visualized in the main panel of Figure 5, the model revealed statistically credible differences when analyzing the underlying odds ratios as seen in the inset of Figure 5. It reinforced the substantially lower odds of success for L-BFGS compared to CG (median OR = 0.2, 95% CrI: [0.09, 0.45]); this relative difference, indicating higher robustness for CG, is subtly reflected in Figure 5 by the slight shift of the L-BFGS probability

distributions (right column) towards lower values compared to CG (left column). The model also showed no credible main effect for rotation removal (median OR = 1.9, 95% CrI: [0.74, 5.07]) nor a credible interaction (median Interaction OR = 1.1, 95% CrI: [0.33, 3.42]), consistent with the high degree of similarity between the top ('no') and bottom ('yes') panels within each optimizer in Figure 5. Thus, while both optimizers perform well on average, the primary factor credibly influencing the relative odds of success in this analysis is the choice of optimizer, with CG demonstrating significantly higher odds of convergence than L-BFGS across both rotation removal settings in this dataset. The large estimated standard deviation for the system-specific random intercepts from the full model (posterior median $\sigma_u = 3.6$, 95% CrI: [2.79, 4.80]) underscores that system-specific properties remain a major determinant of convergence success or failure for individual cases, explaining deviations from the high average success probability. Model diagnostics indicated good convergence and fit (details in SI).

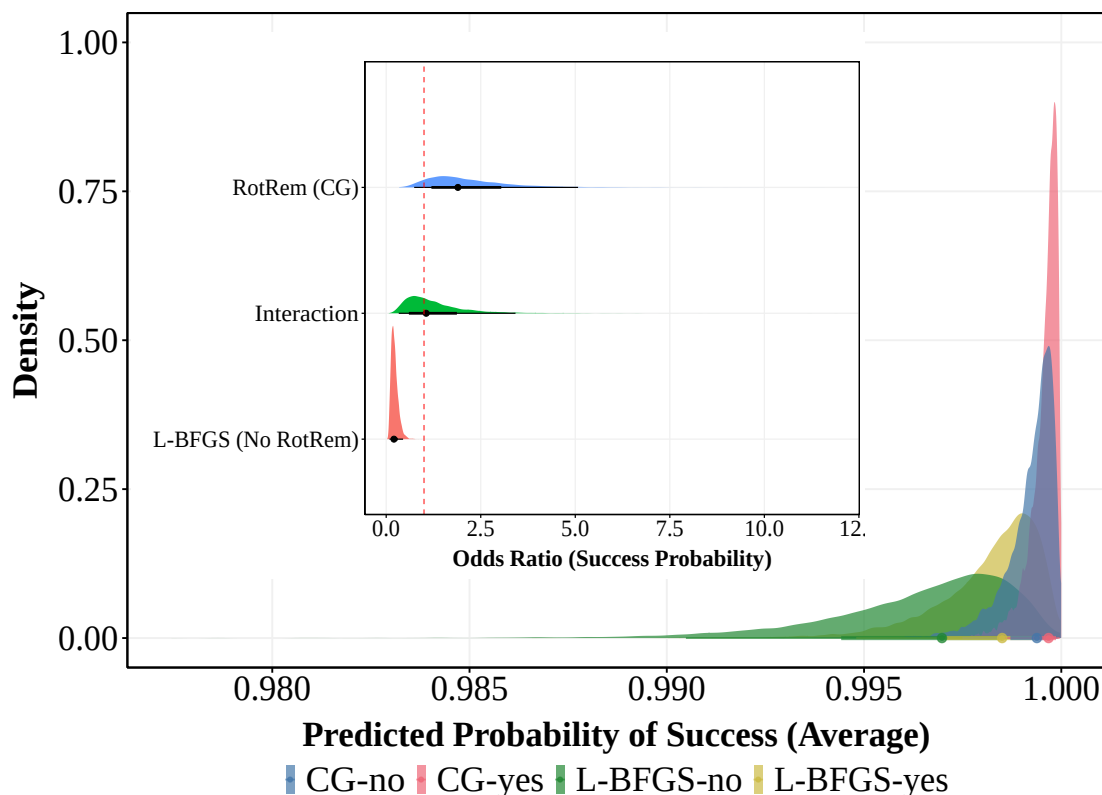


Figure 5: Posterior distributions for convergence success derived from the full interaction model ($\text{brms}_{\text{pfidall}}$). The main panel displays the predicted probability of success for an average system under the four method conditions (Optimizer-Rotation Removal, see legend), illustrating high probabilities (≈ 0.98) for all settings. The inset shows the posterior distributions for the fixed effects on the Odds Ratio (OR) scale relative to the baseline (CG, rotation removal disabled), with the dashed line at $\text{OR}=1$ indicating no change in odds. While absolute probabilities are high, the inset quantifies the relative effects, showing the OR for L-BFGS vs CG (bottom distribution) is credibly below 1, while the ORs for rotation removal (top) and the interaction (middle) credibly include 1. The distributions for CG are slightly shifted towards higher probabilities compared to L-BFGS. Distributions for enabling ('yes') versus disabling ('no') rotation removal are nearly identical within each optimizer column, but do tend to cause a rightward shift. Thick lines in the inset represent 95% credible intervals with median dots.

The preceding analyses provide a quantitative, statistically robust assessment of how the choice of dimer rotation optimizer and the application of rotation removal influence both the computational effort (PES calls) and the likelihood of success for saddle point searches within this benchmark set. Having established these effects and accounted for system-specific variability using Bayesian hierarchical models, we now turn to discussing the implications of these findings in the context of theoretical expectations, practical algorithm choice, and the broader methodology of benchmarking computational chemistry methods.

4 Discussion

Our analysis, employing Bayesian hierarchical models to account for system-specific variability, provides quantitative insights into the performance of CG and L-BFGS optimizers for dimer rotation, and the effect of enabling rotation removal, across a large benchmark set. The key findings indicate a small but credible PES call advantage and significantly higher convergence odds for the CG optimizer compared to L-BFGS. Conversely, enabling rotation removal incurred a substantial PES call penalty without providing a statistically credible improvement in success probability in the full model applied to this dataset.

The superior performance of CG over L-BFGS, particularly its enhanced robustness demonstrated by the success probability analysis (OR for L-BFGS vs CG ≈ 0.2 [0.09, 0.45]), aligns with potential theoretical advantages of CG in navigating complex potential energy surfaces. While modern L-BFGS methods incorporate strategies to ensure positive-definite Hessian approximations [39], they may still be susceptible to challenges in regions with complex curvature compared to methods like CG that directly seek movement along specific eigenmodes [30]. The observed difference in computational effort per successful run was modest (L-BFGS requiring $\sim 2.6\%$ [0.7%, 4.5%] more PES calls than CG when rotation removal was off), suggesting that the primary practical advantage of CG in this context lies in its higher probability of reaching convergence.

Counter-intuitively, enabling rotation removal, theoretically designed to simplify the optimization by removing global rotations of the coordinate vector [33], resulted in a significant increase in computational cost (median +44% PES calls vs disabled) without a corresponding statistically credible improvement in success probability in our full model (OR for RotRem Yes vs No ≈ 1.9 [0.74, 5.07]). This discrepancy likely highlights the sensitivity of optimization performance to implementation details and the specific nature of the PES. The projection involved in rotation removal interacts with the optimizer’s steps and Hessian updates; for this dataset containing potentially fragmenting or aggregating systems near saddle points, where the separation of internal and external coordinates can be ill-defined [38], this projection may hinder convergence pathways that are accessible without it. Thus we observe less efficient trajectories when rotation removal is active for the majority of these systems.

We underscore the value of applying rigorous statistical modeling to computational benchmarks, moving beyond simple averages or qualitative comparisons. Traditional approaches can be easily confounded by the large system-to-system variability inherent in chemical datasets, as evidenced by the substantial standard deviation estimated for the random intercepts in our models i.e. $\sigma_u \approx 0.63$ for PES calls (on the logarithmic scale), $\sigma_{\log} \approx 3.6$ for success odds (on the logit scale). Bayesian hierarchical models explicitly account for this variability through random effects (u_j). Furthermore, they leverage partial pooling (shrinkage), effectively borrowing strength across systems to produce more stable and reliable estimates for the effects of different methods, mitigating the influence of outlier systems - an effect sometimes colloquially related to “regression towards the mean”. This framework also provides direct quantification of uncertainty via full posterior distributions and credible intervals (e.g., Figs. 4, 5), facilitating more nuanced conclusions than point estimates or p-values alone [31, 32]. The ability to model interactions formally is another advantage for dissecting performance factors.

Further theoretical considerations help to contextualize these empirical results. The rotational phase of the Dimer method represents a specialized optimization problem: isolating a single minimum-curvature mode. The Conjugate Gradient algorithm is inherently well-suited for such eigenvector-following tasks. It can also be less susceptible to being trapped by higher-energy eigenpairs during the search [30]. Conversely, while L-BFGS is a highly effective general-purpose optimizer, it does not, in most cases, share the same quadratic convergence guarantees as the full BFGS method [3]. This theoretical background aligns well with our findings, where the most significant performance gap between the two methods appeared in their relative robustness and success rates, rather than in the computational cost of already successful runs.

Given the results, particularly the higher robustness of CG and the general inefficiency introduced by enabling rotation removal in this context, a practical strategy for high-throughput workflows might involve defaulting to the CG optimizer without rotation removal. A fallback mechanism could then activate rotation removal only for specific systems that initially fail to converge, potentially capturing benefits for problematic cases where external modes interfere, although identifying such cases a priori remains challenging. This “chain of methods” approach warrants further study but illustrates how statistically grounded benchmarks can inform practical workflow design beyond simply selecting a single “best” method.

While this study has focused on variants of the Dimer method, the Bayesian hierarchical framework presented here is broadly applicable. An important future direction is its application to a comparative benchmark of fundamentally different classes of algorithms, such as single-ended methods (Dimer, Sella) versus chain-of-states methods (NEB, GSM). Such an analysis could quantitatively address long-standing questions, for example, by modeling the probability of finding the correct path as a function of the number of images in an NEB calculation or comparing the raw

computational cost versus the likelihood of success for finding a transition state starting from only the reactant and product states. This would provide the community with a robust, data-driven basis for selecting the optimal algorithm class for a given high-throughput workflow.

5 Conclusions

We introduced and applied a Bayesian hierarchical modeling framework to rigorously analyze performance metrics from computational chemistry benchmarks, demonstrating its utility for comparing dimer method variants across a large, diverse dataset. This statistically robust approach moves beyond simple averages or visualizations, accounting for system-specific variability and providing nuanced uncertainty quantification, offering a more actionable view for benchmarking algorithms.

Our analysis of the Dimer method variants revealed that for this large benchmark set, the Conjugate Gradient (CG) optimizer for dimer rotation provided a clear advantage in convergence robustness over L-BFGS (Section 2.2). The decision to enable rotation removal is more complex. While theoretically motivated to simplify the potential energy surface, our findings indicate it led to higher computational costs for the majority of systems studied. However, our models also suggest that rotation removal may offer a reliability benefit when paired with the L-BFGS optimizer, highlighting a subtle interplay between algorithmic components that warrants further study.

We assert that these results, along with the automated capabilities of most workflow engines suggest a “chain” of methods approach rather than an absolute best. Although given the slight increase in performance and the significant increase in robustness it is hard to argue for the L-BFGS rotations, the situation for the chemically intuitive external degree of freedom removal is more nuanced.

From the generalized linear mixed models (Section 2.2), using the L-BFGS for rotations showed a small but statistically discernible increase of 3.4% (95% CrI: [1.1%, 5.8%]) in PES calls. Furthermore, the Bernoulli model suggests a substantial improvement in success probability for Dimer CG, with an estimated 23% higher success rate (95% CI: 5%, 40%), supporting the conclusion that CG-rotations are more robust.

There are however, situations where the rotation removal is required for convergence. Since the data demonstrates that for these random saddle point initializations that the rotation removal for such fragmenting systems is not optimal in most cases, it is more natural to first run CG-rotation without external rotation removal, and have a fallback rule to run CG-rotation with external rotation only for systems which otherwise fail. This strategy leverages the higher success rate of CG in the majority of cases while providing a fallback option for more challenging systems.

Our benchmark results and analysis are packaged in a user-friendly repository, showing integration with Snakemake for high throughput calculations and EON for the energy and forces calculation through NWChem along with R code for the figures and running the Bayesian analysis. It is also, to the best of our knowledge, the largest benchmark study done on the modalities of the dimer method. Our analysis provides a more nuanced and statistically robust assessment of performance than traditional approaches, which often rely on simple averages or visualizations that can obscure important details. We expect this reproducible resource will be indispensable to others in the community performing high throughput chemistry or algorithm development.

6 Supplementary Material

Model validations for the Bayesian models are fairly standard and verbose, so they are present in the accompanying supplementary material.

Acknowledgments

This work was supported by the Icelandic Research Fund (grant no. 217436-053).

RG thanks Dr. Miha Gunde, Dr. Amrita Goswami, Dr. Moritz Sallermann, Prof. Debabrata Goswami, Prof. Laurent Karim Béland, Prof. Morris Riedel, Mrs. Sonaly Goswami and Mrs. Ruhila Goswami for discussions. RG also thanks Prof. Normand Mousseau and Prof. Birgir Hrafnkelsson for manuscript suggestions and edits.

Data Availability Statement

The full computational workflow, analysis code, and data supporting this study are openly available. A version-tagged GitHub repository (https://github.com/HaoZeke/brms_idrot_repro) provides all resources needed to

reproduce the findings. To ensure full reproducibility, the repository contains a complete computational environment managed by pixi, with version-pinned software dependencies including EON, NWChem, and ASE, alongside utilities from Wailord [13]. In line with best practices for literate and reproducible programming [15, 17, 18, 44], some dependencies are bundled directly via git-subrepo. For permanent access and citation, the final curated dataset is hosted on the Materials Cloud Archive [46] under the entry (**author?**) [14].

Conflict of interest

The authors declare no conflict of interest.

Appendices

Exact code to reproduce all models is part of the repository.

A Statistical model validation

For details of the specification and interpretation refer to the main text. To ensure the supplementary can be read independently, recall the fixed effect structures i.e.

$$\text{Fixed Effects}_{ij} = \begin{cases} \beta_0 + \beta_1 \text{DR}_{i(j)} & \text{(RotOptimizer)} \\ \beta_0 + \beta_2 \text{RR}_{i(j)} & \text{(RotRemoval)} \\ \beta_0 + \beta_1 \text{DR}_{i(j)} + \beta_2 \text{RR}_{i(j)} + \beta_3 (\text{DR}_{i(j)} \times \text{RR}_{i(j)}) & \text{(Full)} \end{cases} \quad (12)$$

For the analysis below, log-scale parameters mean the direct estimates of the CI from the model summary cannot be used, and instead simulated draws from the posterior are individually exponentiated and then averaged to obtain the point estimates. Details and code for this procedure are in the accompanying Github repository.

A.1 Performance models

A.1.1 Optimizer for the rotation phase

Here we use the (RotOptimizer) subset, i.e. with no rotation removal.

```
Family: negbinomial
Links: mu = log; shape = identity
Formula: pes_calls ~ dimer_rot + (1 | mol_id:spin)
Data: data (Number of observations: 896)
Draws: 4 chains, each with iter = 4000; warmup = 1000; thin = 1;
       total post-warmup draws = 12000

Multilevel Hyperparameters:
~mol_id:spin (Number of levels: 456)
      Estimate Est.Error 1-95%
sd(Intercept)    0.62    0.02    0.58    0.67 1.01    555    1169

Regression Coefficients:
      Estimate Est.Error 1-95%
Intercept         5.69    0.03    5.64    5.75 1.02    286    593
dimer_rotlbfgs    0.03    0.01    0.01    0.04 1.00   24427   8675

Further Distributional Parameters:
      Estimate Est.Error 1-95%
shape    129.21    11.49   108.17   153.03 1.00    6860    8842
```

Draws were sampled using `sample(hmc)`. For each parameter, Bulk_ESS

and Tail_ESS are effective sample size measures, and Rhat is the potential scale reduction factor on split chains (at convergence, Rhat = 1).

The analysis revealed a small, but statistically discernible, difference between the CG and LBFGS algorithms. The estimated coefficient for `dimer_rotlbfgs` was 0.03 (95% CI: 0.01, 0.04). This indicates that the LBFGS method is associated with a slightly higher number of PES calls compared to the CG method.

The random intercept standard deviation (0.62, 95% CI: 0.58, 0.67) is considerably large, suggesting more substantial variability in baseline `pes_calls` across molecule/spin combinations for the IDimer method. The shape parameter of the negative binomial distribution was estimated to be 129.21 (95% CI: 108.17, 153.03), indicating low overdispersion.

Chain convergence was excellent (all Rhat values = 1.00, and all Bulk_ESS and Tail_ESS values were large). Trace plots (Figure 6) confirmed good mixing of the chains.

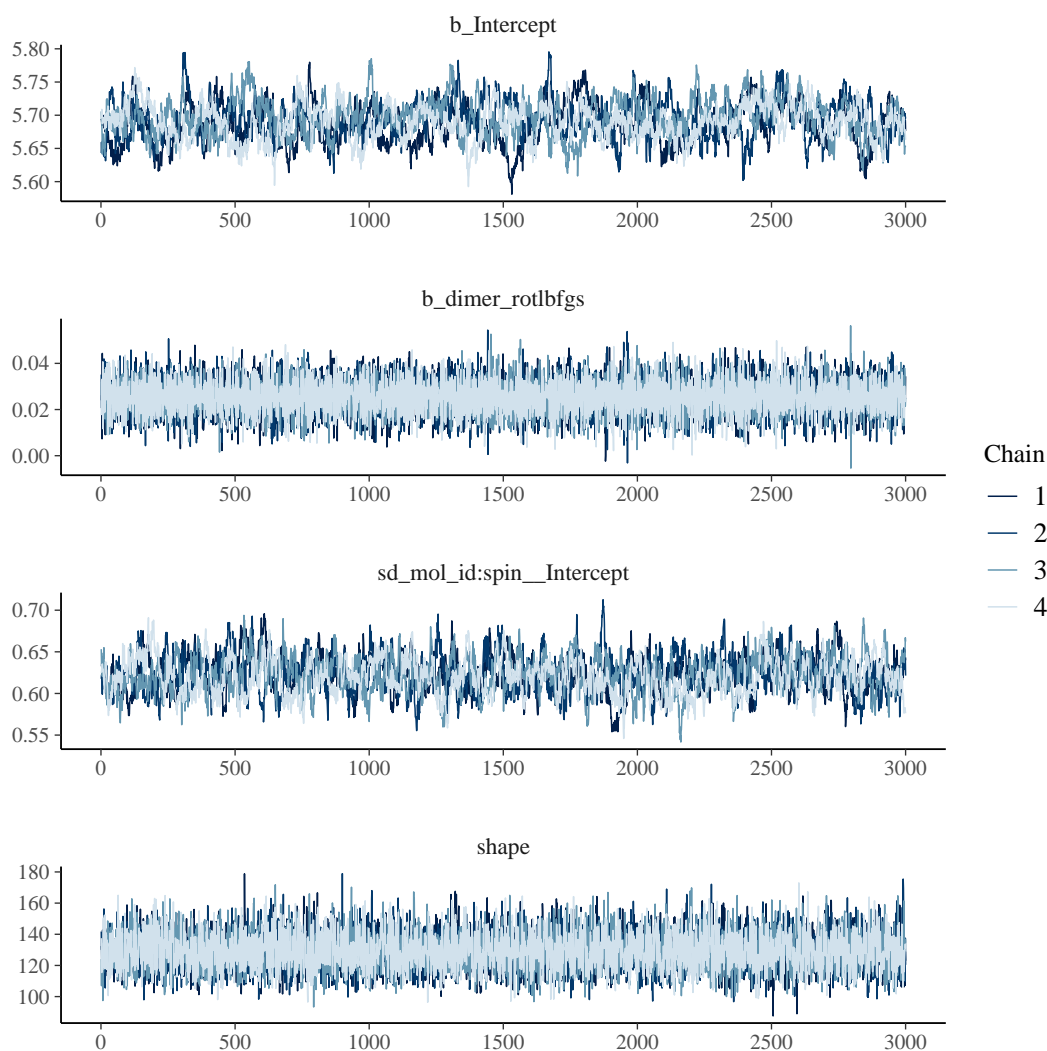


Figure 6: Trace plots for the IDimer CG vs. LBFGS comparison, showing well-mixed chains.

Posterior predictive checks (Figure 7) indicate a good model fit, with the posterior predictive distribution closely matching the observed distribution of `pes_calls`.

The residual error analysis in Figure 8 shows slight heteroscedasticity.

Crucially, the box plot in Figure 9 indicates that there is no systematic bias, so it is good enough for relative comparisons.

The posterior effects including the random effects are summarized in Table 1.

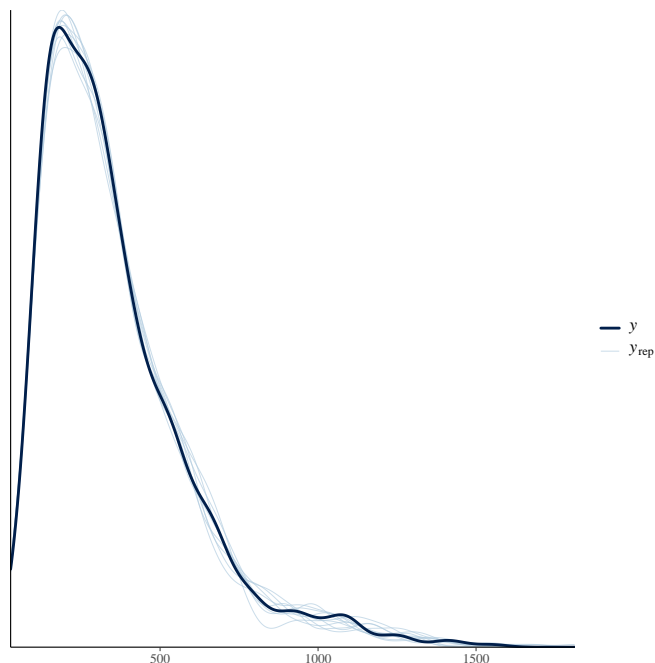


Figure 7: Posterior predictive check for the IDimer CG vs. LBFSG comparison (continuous).

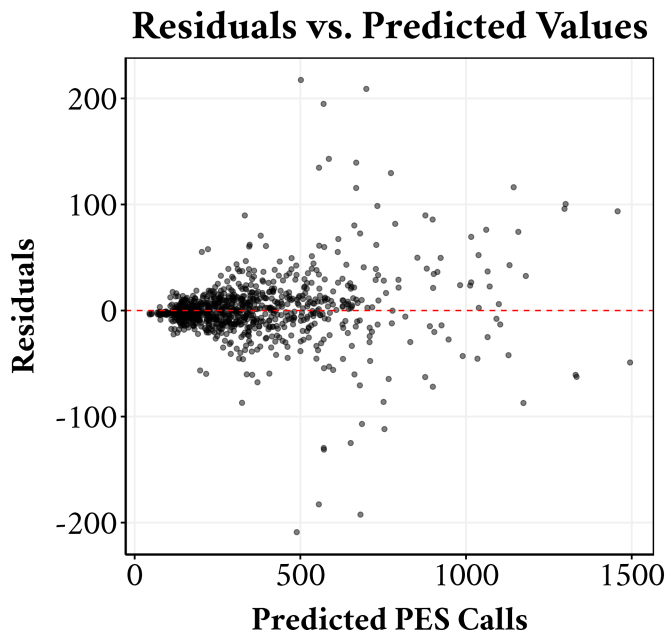


Figure 8: Error residuals for the RotOptimizer subset performance model.

Table 1: RotOptimizer subset performance model effects showing credible intervals

Effect Type	Median Effect	95% CrI
Expected PES Calls (CG, No RotRem)	296.30	[280.5, 313.5]
Multiplicative Factor (L-BFGS vs CG)	1.03	[1.01, 1.04]
Percentage Change (L-BFGS vs CG)	2.6%	[1.1%, 4.1%]
sd(Intercept) [molid:spin]	0.62	[0.58, 0.67]

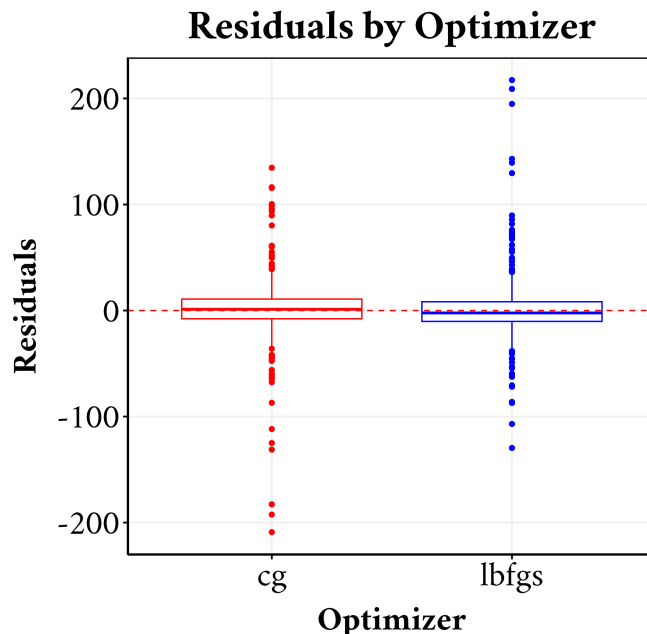


Figure 9: Boxplot of the error residuals for the RotOptimizer subset performance model, showing no bias.

A.1.2 Removal of external rotation

This model is fit to the RotRemoval subset, with the CG optimizer, as it is the better of the two from the previous section.

```
Family: negbinomial
Links: mu = log; shape = identity
Formula: pes_calls ~ rot_removal + (1 | mol_id:spin)
Data: data (Number of observations: 971)
Draws: 4 chains, each with iter = 4000; warmup = 1000; thin = 1;
total post-warmup draws = 12000
```

Multilevel Hyperparameters:

```
~mol_id:spin (Number of levels: 492)
      Estimate Est.Error 1-95%
sd(Intercept)    0.66    0.02   0.62    0.71 1.01    1253    1380
```

Regression Coefficients:

```
      Estimate Est.Error 1-95%
Intercept    5.76    0.03   5.70    5.82 1.01     695    1593
rot_removalyes 0.35    0.01   0.33    0.37 1.00    25842   8962
```

Further Distributional Parameters:

```
      Estimate Est.Error 1-95%
shape    44.35    3.06   38.58   50.53 1.00    6202    9190
```

Draws were sampled using `sample(hmc)`. For each parameter, `Bulk_ESS` and `Tail_ESS` are effective sample size measures, and `Rhat` is the potential scale reduction factor on split chains (at convergence, `Rhat = 1`).

The analysis revealed a large, statistically discernible, difference between choosing to use external rotation removal. The estimated coefficient for `rot_removalyes` was 0.35 (95% CI: 0.33, 0.37). This indicates that the removal of external rotations is associated with a significantly higher number of PES calls compared to not using the rotation removal.

The random intercept standard deviation (0.66, 95% CI: 0.62, 0.71) is considerably large, suggesting more substantial variability in baseline $\text{pes}_{\text{calls}}$ across molecule/spin combinations for the dimer method. The shape parameter of the negative binomial distribution was estimated to be 44 (95% CI: 38.58, 50.53), indicating high overdispersion.

Chain convergence was excellent (all Rhat values ~ 1.00 , and all Bulk_{ESS} and Tail_{ESS} values were large). Trace plots (Figure 10) confirmed good mixing of the chains.

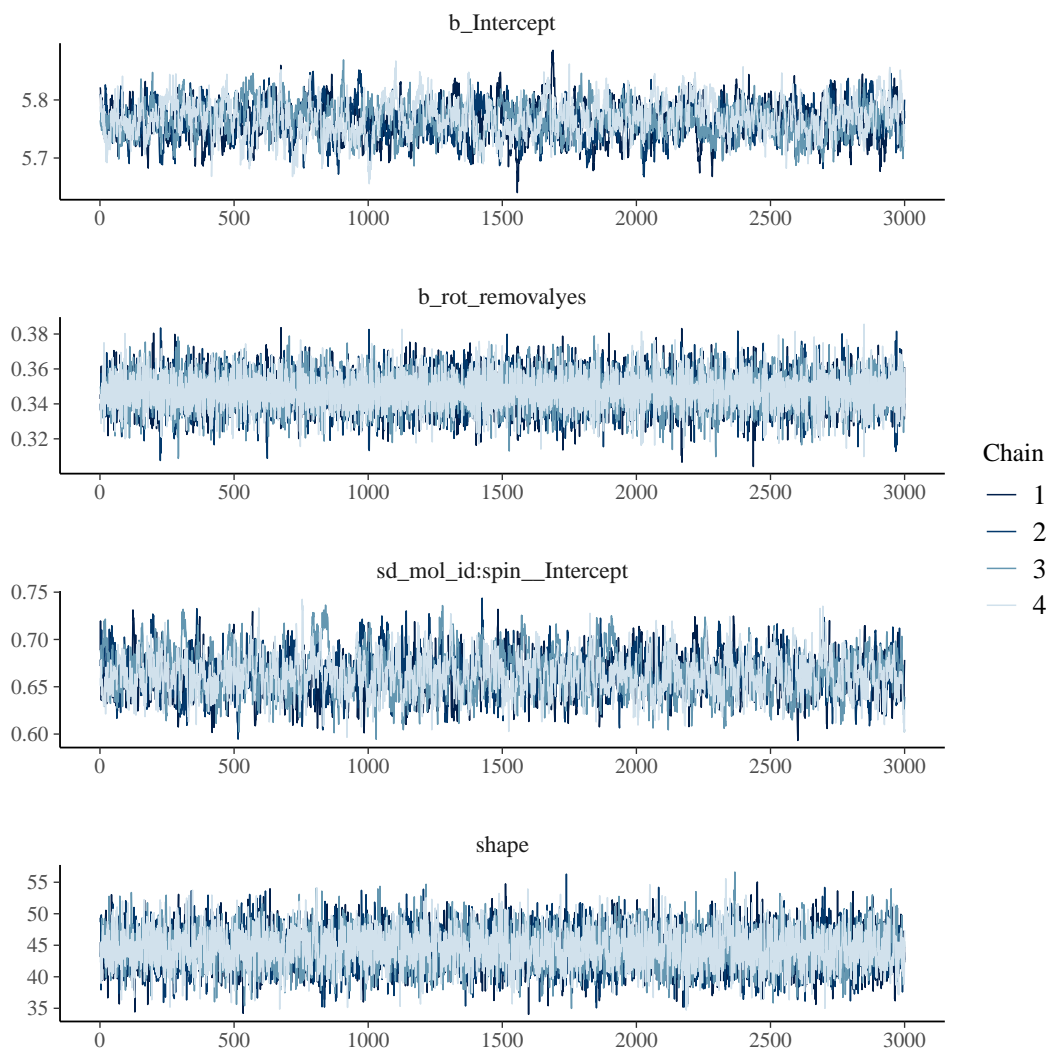


Figure 10: Trace plots for the rotation removal comparison, showing well-mixed chains.

Posterior predictive checks (Figure 11) indicate a good model fit, with the posterior predictive distribution closely matching the observed distribution of $\text{pes}_{\text{calls}}$.

The residual error analysis in Figure 12 shows slight heteroscedasticity, but less than the optimizer subset.

As before, the box plot in 13 indicates that there is no systematic bias, so it is good enough for relative comparisons.

The posterior effects including the random effects are summarized in Table 2.

A.1.3 Combined model

To use all the data generated and draw the inferences in the main text, we fit a full hierarchical model.

```
Family: negbinomial
Links: mu = log; shape = identity
```

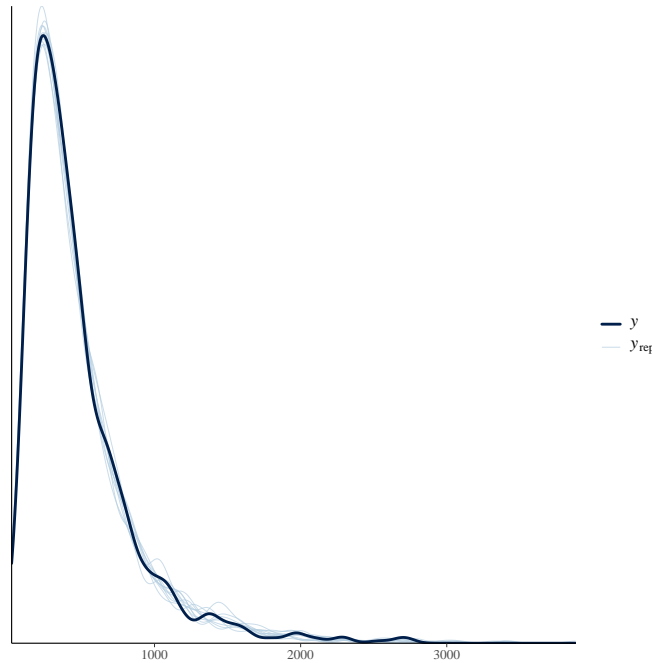


Figure 11: Posterior predictive check for the rotation removal comparison (continuous).

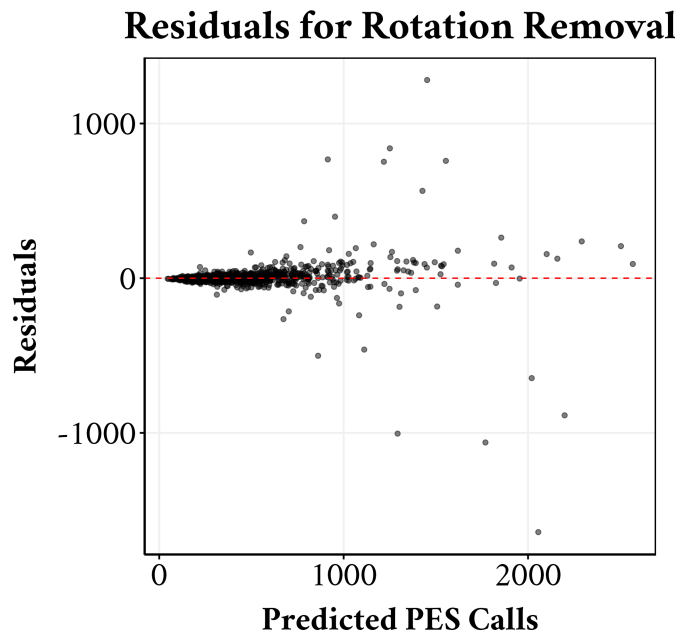


Figure 12: Error residuals for the RotRemoval subset performance model.

Table 2: RotRemoval subset performance model effects, including credible intervals.

Effect Type	Median Effect	95% CrI
Expected PES Calls (CG, No RotRem)	318.70	[300.3, 338.1]
Multiplicative Factor (RotRem vs No RotRem)	1.41	[1.39, 1.44]
Percentage Change (RotRem vs No RotRem)	41.5%	[38.6%, 44.4%]
sd(Intercept) [molid:spin]	0.66	[0.62, 0.71]

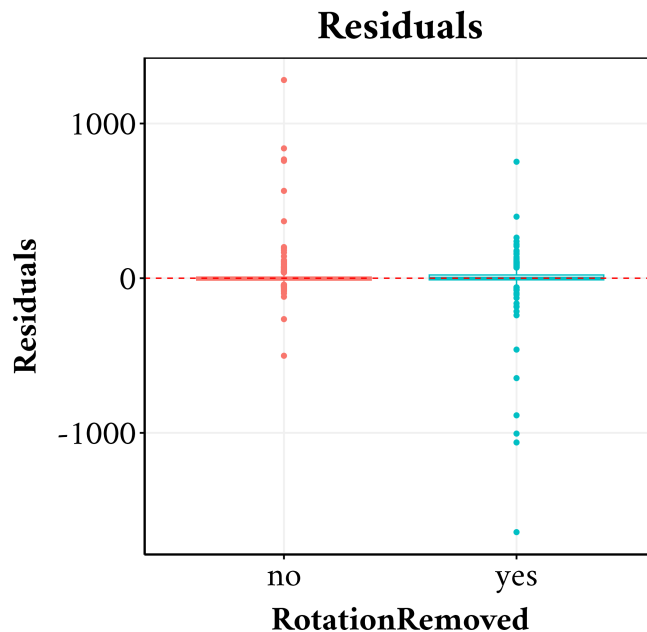


Figure 13: Boxplot of the error residuals for the RotRem subset performance model, showing no bias.

```
Formula: pes_calls ~ dimer_rot * rot_removal + (1 | mol_id:spin)
Data: data (Number of observations: 1805)
Draws: 4 chains, each with iter = 4000; warmup = 1000; thin = 1;
total post-warmup draws = 12000
```

Multilevel Hyperparameters:

```
~mol_id:spin (Number of levels: 458)
      Estimate Est.Error l-95%
sd(Intercept)    0.63    0.02    0.59    0.67 1.01    314    1104
```

Regression Coefficients:

	Estimate	Est.Error	l-95%				
Intercept	5.69	0.03	5.63	5.75	1.02	173	333
dimer_rotlbfgs	0.03	0.01	0.01	0.04	1.00	7773	8783
rot_removalyes	0.37	0.01	0.35	0.38	1.00	7986	8829
dimer_rotlbfgs:rot_removalyes	0.01	0.01	-0.01	0.04	1.00	6672	8277

Further Distributional Parameters:

	Estimate	Est.Error	l-95%			
shape	63.99	2.75	58.70	69.59	1.00	11187 8962

Draws were sampled using `sample(hmc)`. For each parameter, `Bulk_ESS` and `Tail_ESS` are effective sample size measures, and `Rhat` is the potential scale reduction factor on split chains (at convergence, `Rhat` = 1).

The combined model reinforces the findings from the subset models and provides a more nuanced understanding of the factors influencing the number of PES calls.

The main effect for the L-BFGS optimizer (`dimer_rotlbfgs`) is estimated at 0.03 (95% CI: [0.01, 0.04]), consistent with the RotOptimizer subset model. This confirms that, holding rotation removal constant, the L-BFGS optimizer is associated with a small but discernible increase in `pes_calls` compared to the Conjugate Gradient (CG) optimizer.

Similarly, the main effect for enabling the removal of external rotations (`rot_removalyes`) is 0.37 (95% CI: [0.35, 0.38]). This indicates a substantial and statistically significant increase in `pes_calls` when rotation removal is active, compared to when it is not, holding the choice of optimizer constant. This represents a performance cost of approximately 45%.

Crucially, the interaction term `dimer_rotlbfgs:rot_removalyes` is very small (0.01) and its 95% CI ([-0.01, 0.04]) overlaps with zero. This suggests that there is no discernible interaction effect. In practical terms, the slight performance decrease from using L-BFGS instead of CG is consistent, regardless of whether external rotation removal is used or not.

The random intercept standard deviation remains large at 0.63 (95% CI: [0.59, 0.67]), again highlighting significant baseline variability in `pes_calls` across different molecular systems. The shape parameter is estimated at 63.99, indicating moderate overdispersion in the data.

Model diagnostics were excellent. All `Rhat` values are close to 1.0, and the `Bulk_ESS` and `Tail_ESS` values are large, indicating that the Markov chains converged and mixed well. Trace plots (Figure 14) confirmed good mixing of the chains.

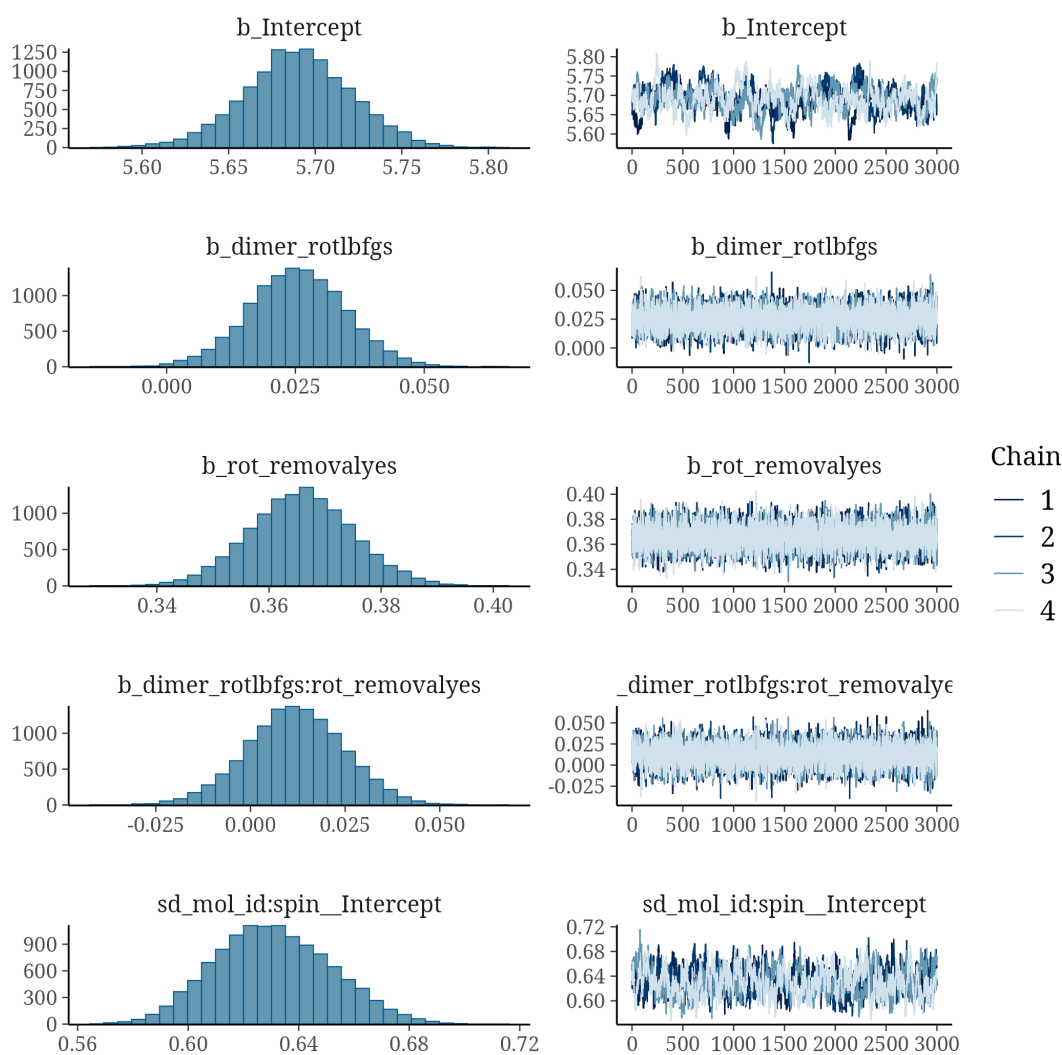


Figure 14: Trace plots for the main parameters of the combined performance model showing well-mixed chains.

Posterior predictive checks (Figure 15) indicate a good model fit, with the posterior predictive distribution closely matching the observed distribution of `pes_calls`.

The residual error analysis in Figure 16 shows slight heteroscedasticity, but less than the optimizer subset.

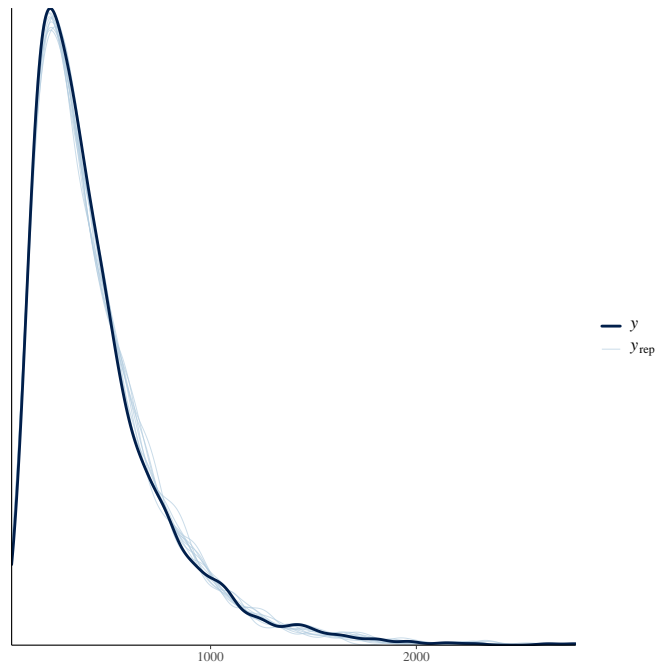


Figure 15: Posterior predictive check for the combined performance model (continuous).

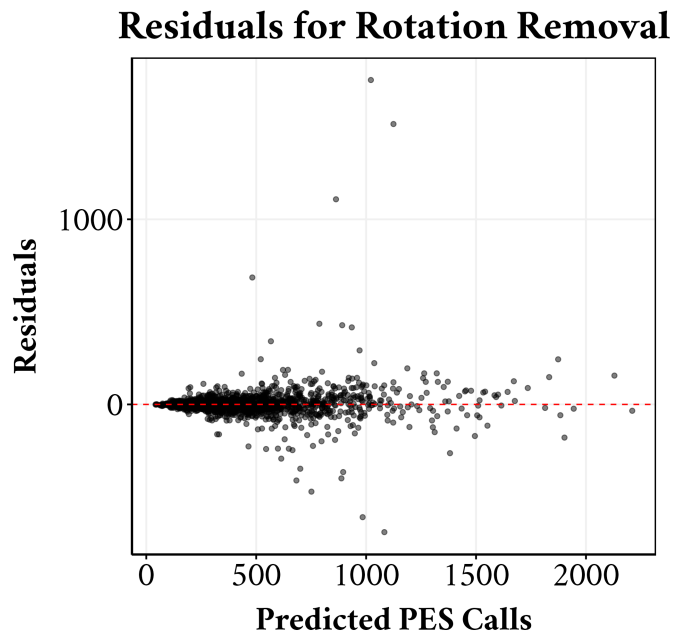


Figure 16: Error residuals for the combined performance model.

As before, the box plot in 17 indicates that there is no systematic bias, so it is good enough for relative comparisons.

Residuals by Optimizer and Rotation R

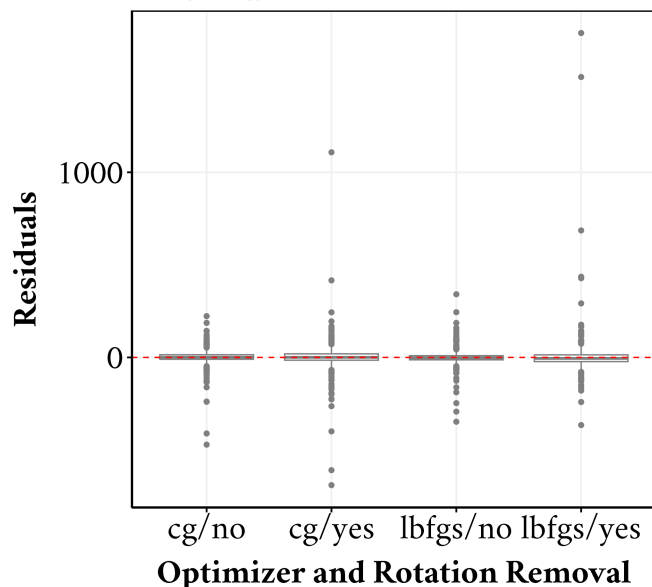


Figure 17: Boxplot of the error residuals for the combined performance model, showing no bias.

The posterior effects including the random effects are summarized in Table 3.

Table 3: Performance model effects, including credible intervals.

Effect Type	Median Effect	95% CrI
Expected PES Calls (CG, No RotRem)	295.90	[278.0, 314.6]
Multiplicative Factor (L-BFGS vs CG / No RotRem)	1.03	[1.01, 1.04]
Percentage Change (L-BFGS vs CG / No RotRem)	2.6%	[0.7%, 4.5%]
Multiplicative Factor (RotRem Yes vs No / CG)	1.44	[1.42, 1.47]
Percentage Change (RotRem Yes vs No / CG)	44.2%	[41.6%, 46.8%]
Multiplicative Factor (Interaction)	1.01	[0.99, 1.04]
Percentage Change (Interaction)	1.2%	[-1.4%, 3.8%]
sd(Intercept) [molid:spin]	0.63	[0.59, 0.67]

In summary, the full model provides robust evidence that for optimizing the number of `pes_calls`, the Conjugate Gradient (CG) optimizer should be preferred over L-BFGS, and external rotation removal should be disabled. The absence of an interaction effect simplifies the conclusion: these two choices are independent, and the optimal combination is CG without rotation removal.

A.2 Total time model

Here we demonstrate the result of a combined total time model. As noted in the main text, the interpretation of this model shows that it is largely a proxy for the PES call performance, despite the difference in model family (Gamma compared to NegBinomial, due to continuous time data over discrete PES calls).

```
Family: gamma
Links: mu = log; shape = identity
Formula: tot_time ~ dimer_rot * rot_removal + (1 | mol_id:spin)
Data: data (Number of observations: 1805)
Draws: 4 chains, each with iter = 4000; warmup = 1000; thin = 1;
total post-warmup draws = 12000
```

Multilevel Hyperparameters:

```

~mol_id:spin (Number of levels: 458)
      Estimate Est.Error 1-95%
sd(Intercept)    0.66    0.02  0.61    0.70 1.01    326    687

```

Regression Coefficients:

```

      Estimate Est.Error 1-95%
Intercept          3.10    0.03  3.03    3.16 1.03    169
dimer_rotlbfgs     0.03    0.01  0.01    0.04 1.00   8956
rot_removalyes     0.36    0.01  0.34    0.38 1.00   8554
dimer_rotlbfgs:rot_removalyes 0.01    0.01 -0.02    0.04 1.00   7661
      Tail_ESS
Intercept          288
dimer_rotlbfgs    9686
rot_removalyes    9371
dimer_rotlbfgs:rot_removalyes 8711

```

Further Distributional Parameters:

```

      Estimate Est.Error 1-95%
shape    51.85    1.97  48.06    55.80 1.00   10773    9266

```

Draws were sampled using `sample(hmc)`. For each parameter, `Bulk_ESS` and `Tail_ESS` are effective sample size measures, and `Rhat` is the potential scale reduction factor on split chains (at convergence, `Rhat` = 1).

The analysis of the Gamma model for total wall time (`tot_time`) reveals a narrative remarkably consistent with the `pes_calls` performance model. The estimated coefficients for the predictors are nearly identical to those in the negative binomial model.

The effect for `dimer_rotlbfgs` is 0.03 (95% CI: [0.01, 0.04]), and for `rot_removalyes` it is 0.36 (95% CI: [0.34, 0.38]). As with the `pes_calls` model, the interaction term remains small and not statistically discernible, with a coefficient of 0.01 and a 95% CI of [-0.02, 0.04] that comfortably includes zero. This striking similarity confirms that the total wall time is predominantly driven by the number of PES calls required for convergence.

The random intercept standard deviation of 0.66 (95% CI: [0.61, 0.70]) is also very similar to the combined `pes_calls` model, indicating that molecules that are intrinsically more difficult (requiring more PES calls) also take proportionally longer to compute.

Model diagnostics were excellent, as before. All `Rhat` values are close to 1.0, and the `Bulk_ESS` and `Tail_ESS` values are large, indicating that the Markov chains converged and mixed well. Trace plots (Figure 18) confirmed good mixing of the chains.

Posterior predictive checks (Figure 19) indicate a good model fit, with the posterior predictive distribution closely matching the observed distribution of `tot_time`.

The residual error analysis in Figure 20 shows slight heteroscedasticity, but less than the optimizer subset.

As before, the box plot in 21 indicates that there is no systematic bias, so it is good enough for relative comparisons.

The posterior effects including the random effects are summarized in Table 4.

Table 4: Total time model effects, including credible intervals.

Effect Type	Median Effect	95% CrI
Expected Wall Time (CG, No RotRem)	22.20	[20.8, 23.7]
Multiplicative Factor (L-BFGS vs CG / No RotRem)	1.03	[1.01, 1.04]
Percentage Change (L-BFGS vs CG / No RotRem)	2.6%	[0.7%, 4.5%]
Multiplicative Factor (RotRem Yes vs No / CG)	1.43	[1.40, 1.46]
Percentage Change (RotRem Yes vs No / CG)	43.0%	[40.4%, 45.6%]
Multiplicative Factor (Interaction)	1.01	[0.98, 1.04]
Percentage Change (Interaction)	1.0%	[-1.6%, 3.6%]
sd(Intercept) [molid:spin]	0.66	[0.61, 0.70]

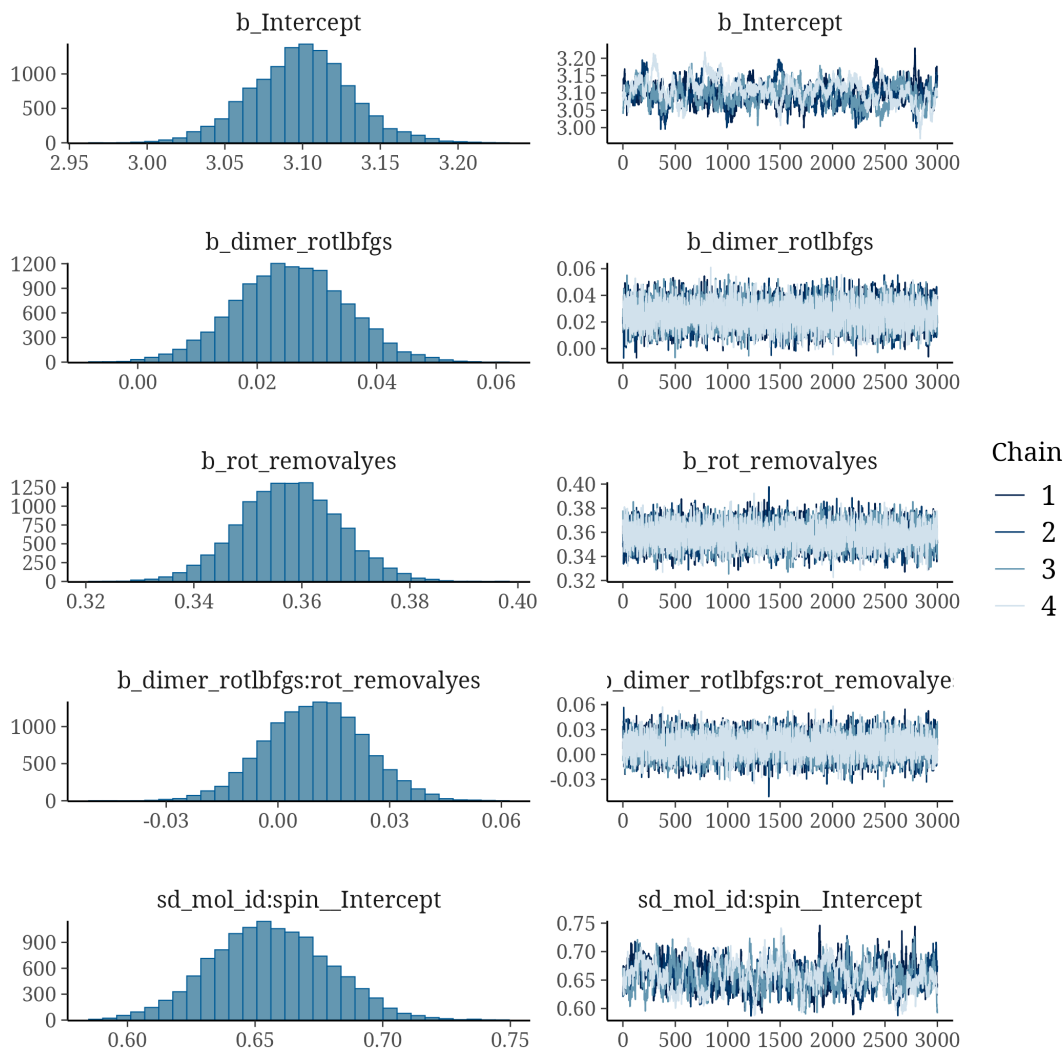


Figure 18: Trace plots for the main parameters of the combined time model showing well-mixed chains.

This model serves as a real-world validation of the conclusions drawn from the performance model. The most efficient method in terms of computational steps (CG optimizer, no rotation removal) is also the fastest in terms of total wall time.

A.3 Success modeling

To assess the relative reliability of each setting, we model the probability of a successful calculation using a hierarchical logistic regression model. Success is a binary outcome (1 for success, 0 for failure).

A.3.1 Optimizer for the rotation phase

Here we use the (RotOptimizer) subset, i.e. with no rotation removal.

```
Family: bernoulli
Links: mu = logit
Formula: success ~ dimer_rot + (1 | mol_id:spin)
Data: data (Number of observations: 1000)
Draws: 4 chains, each with iter = 4000; warmup = 1000; thin = 1;
total post-warmup draws = 12000
```

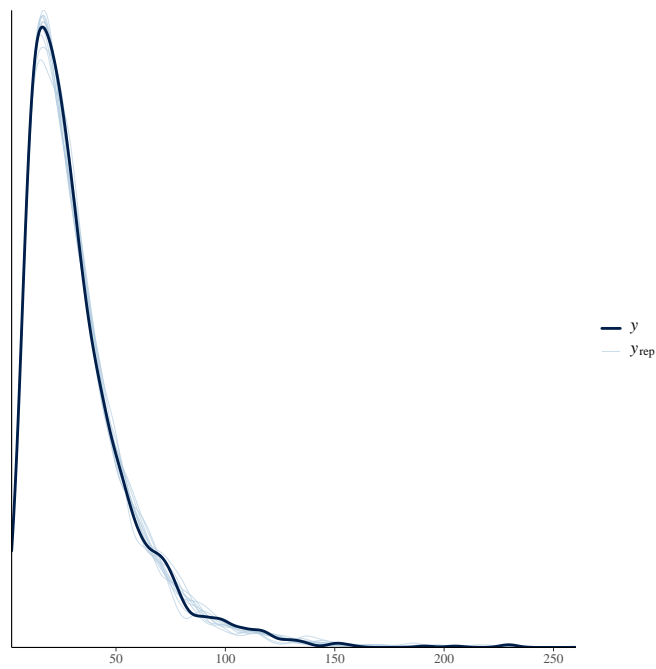


Figure 19: Posterior predictive check for the combined time model (continuous).

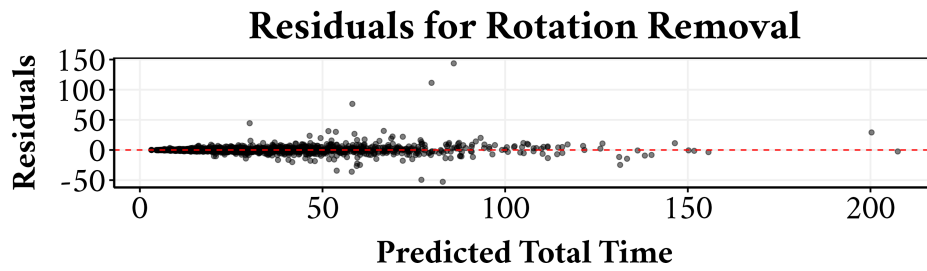


Figure 20: Error residuals for the combined time model.

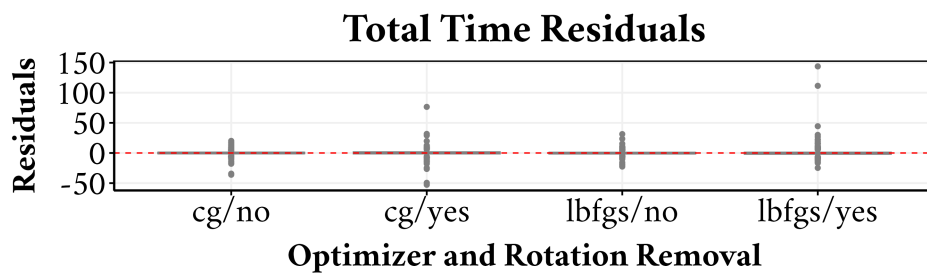


Figure 21: Boxplot of the error residuals for the combined time model, showing no bias.

Multilevel Hyperparameters:

```
~mol_id:spin (Number of levels: 500)
      Estimate Est.Error 1-95%
sd(Intercept)    2.61    0.55    1.67    3.81 1.00    2719    5242
```

Regression Coefficients:

```
      Estimate Est.Error 1-95%
Intercept    5.80    0.84    4.40    7.72 1.00    3336    5181
dimer_rotlbfgs -1.25    0.39    -2.06   -0.52 1.00    11747    8823
```

Draws were sampled using `sample(hmc)`. For each parameter, `Bulk_ESS` and `Tail_ESS` are effective sample size measures, and `Rhat` is the potential scale reduction factor on split chains (at convergence, `Rhat = 1`).

In absolute terms, both optimizers are highly reliable. Based on the model’s median intercept, the typical probability of success for the baseline CG optimizer is extremely high at $\approx 99.7\%$. For the L-BFGS optimizer, the success rate also remains very high at $\approx 99.0\%$.

Despite these high absolute rates, the statistical model is detects a robust relative difference between the two. The coefficient for `dimer_rotlbfgs` is -1.25 (95% CI: $[-2.06, -0.52]$), indicating a statistically discernible difference in the log-odds of success.

Model diagnostics were excellent. All `Rhat` values are close to 1.0, and the `Bulk_ESS` and `Tail_ESS` values are large, indicating that the Markov chains converged and mixed well. Trace plots (Figure 22) confirmed good mixing of the chains.

Posterior predictive checks (Figure 23) indicate a good model fit, with the posterior predictive distribution closely matching the observed distribution of success.

Further diagnostics were performed using the DHARMA package, which creates standardized residuals for complex models. The results in Figure 24 are excellent and support the validity of the model.

QQ plot (left panel) This plot compares the empirical distribution of residuals against the expected uniform distribution. The points lie almost perfectly along the diagonal line, indicating that the model’s residuals are distributed as expected. This visual finding is supported by formal statistical tests for correct distribution (Kolmogorov-Smirnov test, $p=0.62$), correct dispersion ($p=0.99$), and outliers ($p=1$), none of which show a significant deviation.

Residuals vs. Predictors (right panel) This plot checks for non-uniform patterns in the residuals across the two optimizer groups. The boxplots are centered around the expected median of 0.5 and have similar spreads. The non-significant Levene Test confirms that the variance of the residuals is homogeneous across the groups.

The practical meaning of this relative difference is best understood through the odds ratios summarized in Table 5. While both methods nearly always succeed, the odds of success are substantially different. The odds ratio for L-BFGS relative to CG is just 0.29, which corresponds to a median change in the odds of success of -70.9% (95% CrI: $[-87.2\%, -40.4\%]$).

Table 5: RotOptimizer success model effects, including credible intervals.

Effect Type	Median Effect	95% CrI
Probability (CG Success)	1.00	[0.99, 1.00]
Odds Ratio (L-BFGS vs. CG)	0.29	[0.13, 0.60]
sd(Intercept) [molid:spin]	2.56	[1.67, 3.81]

Framed differently, an odds ratio of 0.29 indicates that the odds of failure, though small for both, are over three times higher for L-BFGS than for CG ($1 / 0.29 \approx 3.45$). Therefore, while both methods are very effective, the analysis shows that the CG optimizer is the more robust and reliable choice when external rotation is not being removed.

A.3.2 Removal of external rotation

This model is fit to the RotRemoval subset, with the CG optimizer, as it is the better of the two from the previous section.

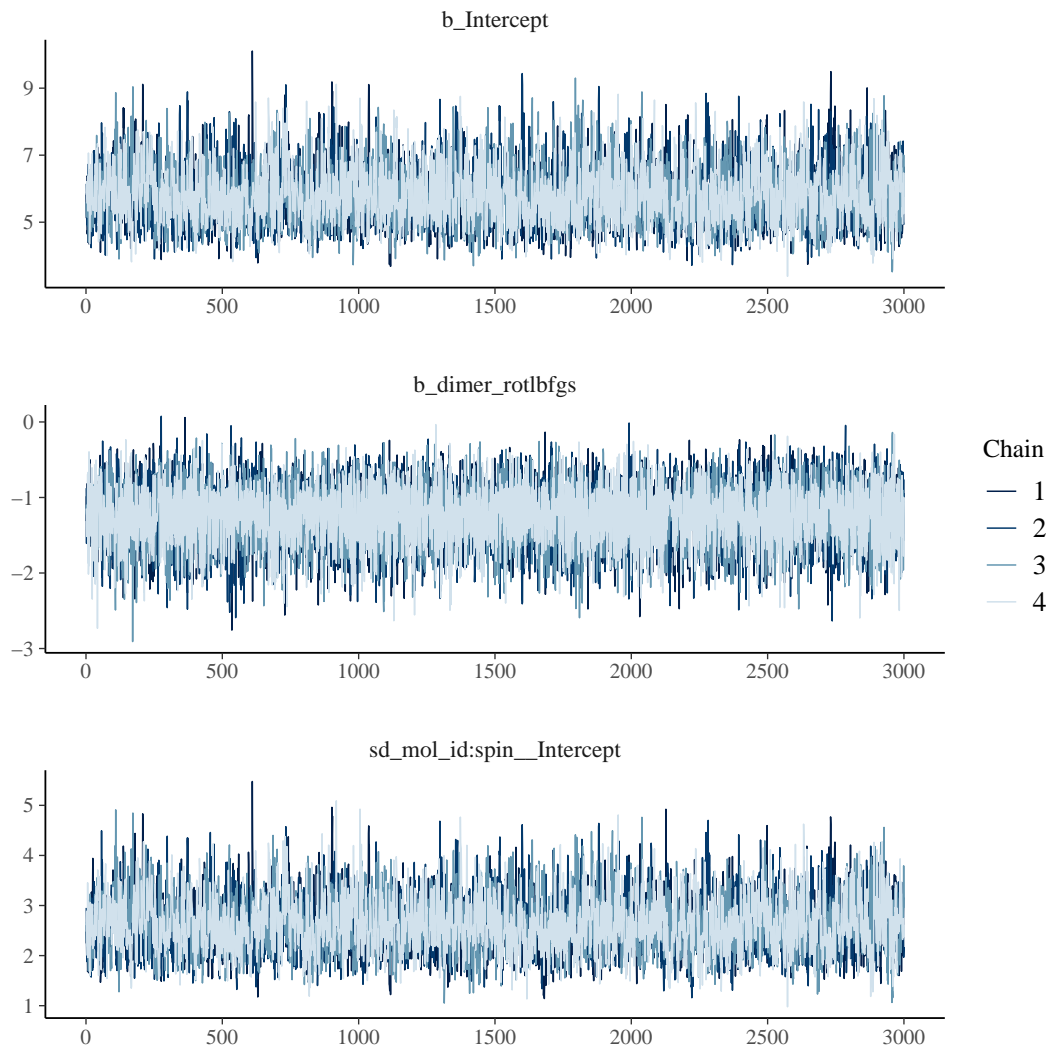


Figure 22: Trace plots for the main parameters of the RotOptimizer success model, showing well-mixed chains.

```

Family: bernoulli
Links: mu = logit
Formula: success ~ rot_removal + (1 | mol_id:spin)
Data: data (Number of observations: 1000)
Draws: 4 chains, each with iter = 4000; warmup = 1000; thin = 1;
       total post-warmup draws = 12000
    
```

Multilevel Hyperparameters:

```

~mol_id:spin (Number of levels: 500)
      Estimate Est.Error l-95%
sd(Intercept)    4.36    1.12    2.63    6.91 1.00    2997    4643
    
```

Regression Coefficients:

```

      Estimate Est.Error l-95%
Intercept    8.66    1.90    5.81   13.12 1.00    3157    4678
rot_removalyes 0.72    0.55   -0.31    1.85 1.00   14155    8596
    
```

Draws were sampled using `sample(hmc)`. For each parameter, Bulk_ESS

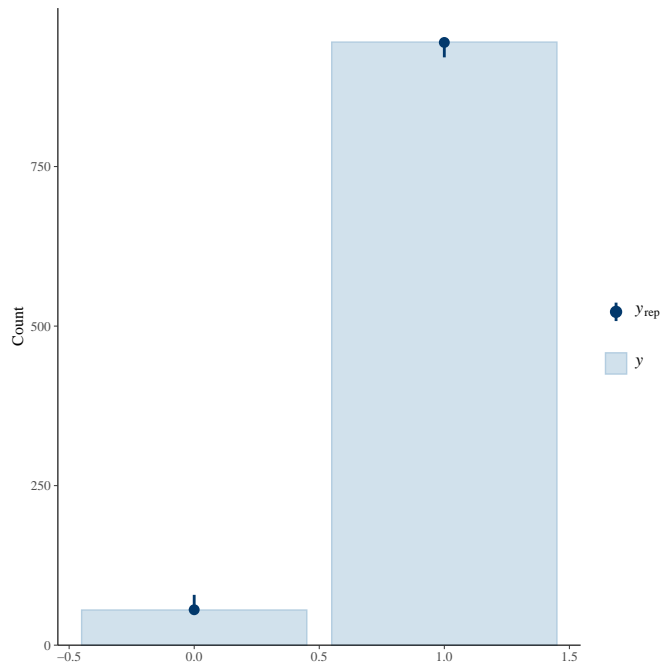


Figure 23: Posterior predictive check for the RotOptimizer success model.

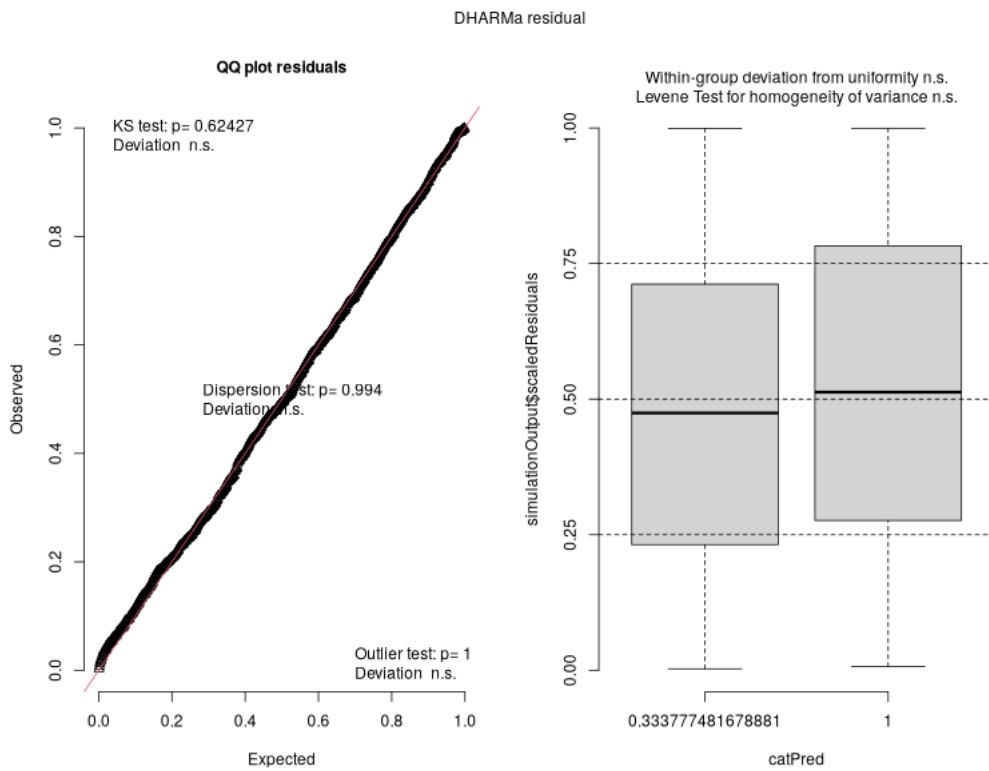


Figure 24: DHARMA diagnostic plots for the RotOptimizer success model, showing a good fit with no significant deviations in residuals.

and Tail_ESS are effective sample size measures, and Rhat is the potential scale reduction factor on split chains (at convergence, Rhat = 1).

The key finding from this model is that there is no evidence of a discernible effect. The coefficient for rot_removalyes is 0.72, but its 95% CI [-0.31, 1.85] broadly overlaps with zero. This indicates that we cannot confidently conclude that enabling rotation removal has any impact—positive or negative—on the success rate.

It is also important to note that the baseline success rate (with the CG optimizer and no rotation removal) is already effectively 100%, as indicated by the massive intercept of 8.66. When a process is already so reliable, it is difficult for a modification to show a measurable improvement.

Model diagnostics were excellent. All Rhat values are close to 1.0, and Bulk_ESS and Tail_ESS values are large, indicating good chain convergence.

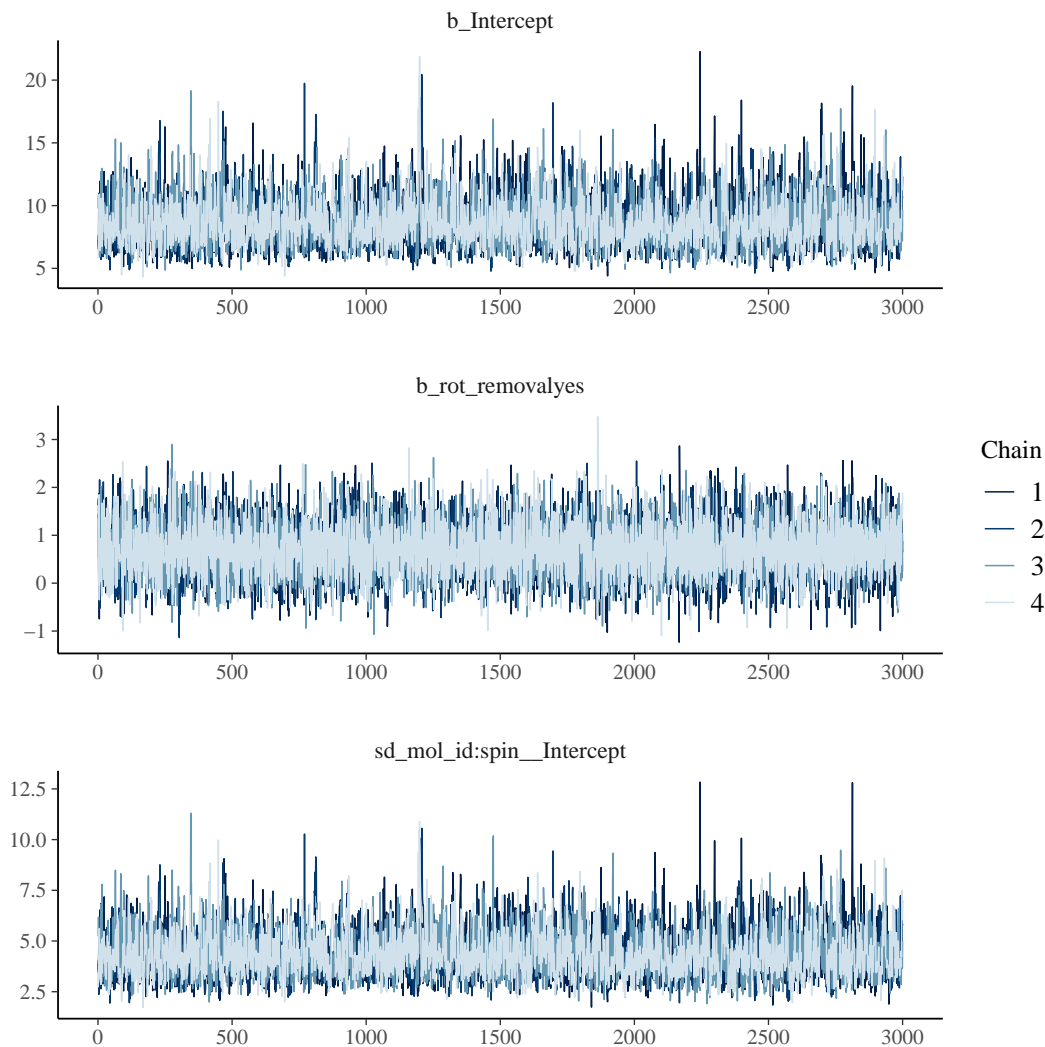


Figure 25: Trace plots for the main parameters of the RotRemoval success model, showing well-mixed chains.

Posterior predictive checks (Figure 26) indicate a good model fit, with the posterior predictive distribution closely matching the observed distribution of success.

The DHARMA diagnostic plots in Figure 27 further support the model's validity. The QQ plot's points fall along the diagonal, and the formal tests for deviation are all non-significant (e.g., KS test, $p=0.86$; Dispersion test, $p=0.95$), indicating correctly distributed residuals.

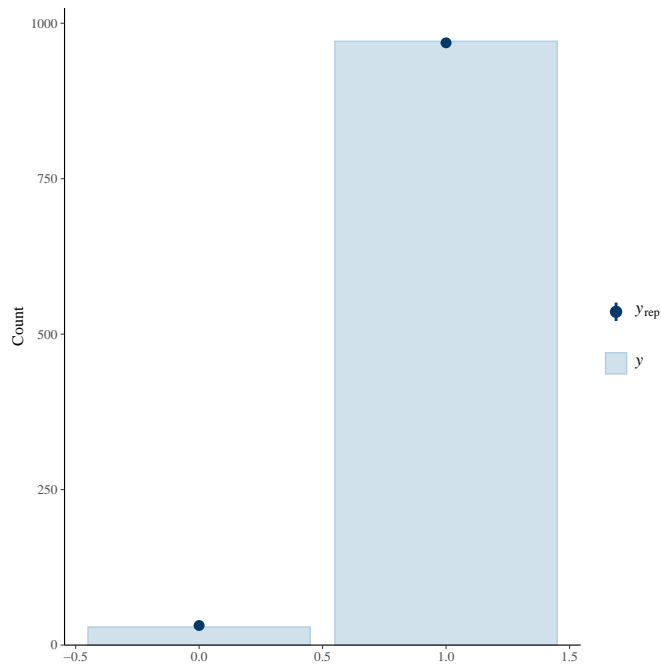


Figure 26: Posterior predictive check for the RotRemoval success model.

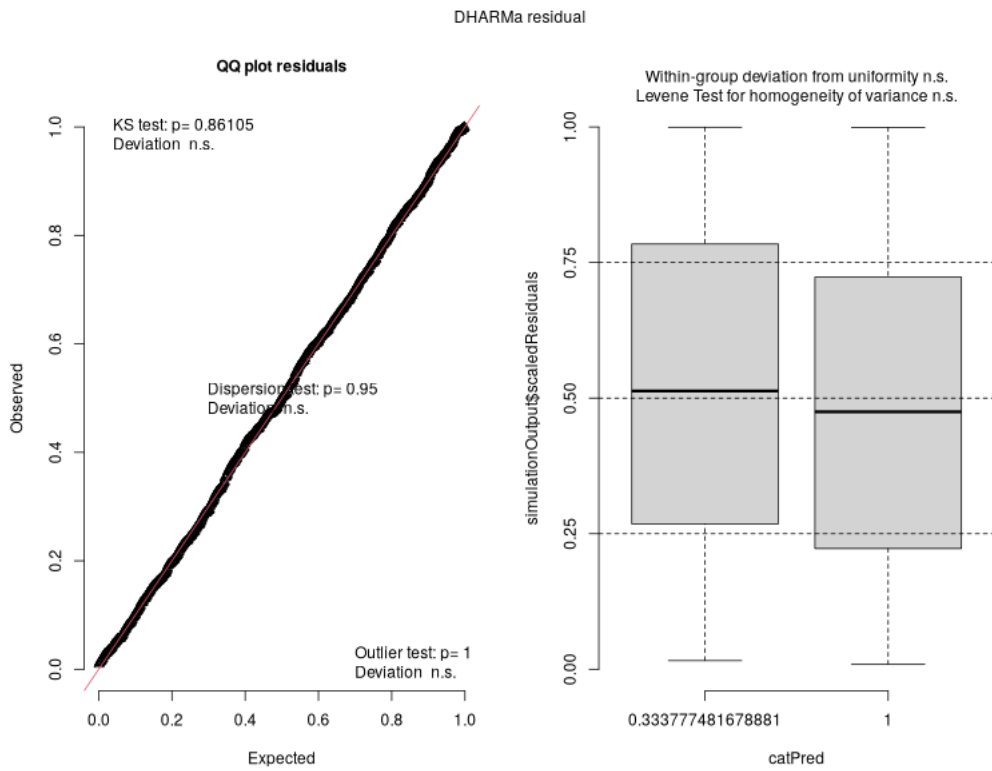


Figure 27: DHARMA diagnostic plots for the RotRemoval success model, showing a good fit.

This statistical uncertainty is clearly reflected in the summary table (Table 6). While the median Odds Ratio for using rotation removal is 2.0, suggesting it might double the odds of success, the 95% credible interval [0.73, 6.35] is extremely wide. Since the interval contains 1.0 (no change in odds), we cannot rule out the possibility of no effect or even a slight negative effect.

Table 6: RotRemoval success model effects, including credible intervals.

Effect Type	Median Effect	95% CrI
Probability (CG Success)	1.0	[1.00, 1.00]
Odds Ratio RotRemove (Yes vs. No)	2.0	[0.73, 6.35]
sd(Intercept) [molid:spin]	3.6	[2.79, 4.80]

In sharp contrast to the clear and practical impact of the optimizer choice, this analysis provides no evidence to suggest that enabling or disabling external rotation removal has a discernible effect on the ultimate success of a calculation.

A.3.3 Combined model

To verify the findings from the subset models and test for any interaction effects, a full model incorporating both the optimizer choice and rotation removal setting was fit to all available data.

```
Family: bernoulli
Links: mu = logit
Formula: success ~ dimer_rot * rot_removal + (1 | mol_id:spin)
Data: data (Number of observations: 2000)
Draws: 4 chains, each with iter = 4000; warmup = 1000; thin = 1;
total post-warmup draws = 12000
```

Multilevel Hyperparameters:

```
~mol_id:spin (Number of levels: 500)
      Estimate Est.Error 1-95%
sd(Intercept)    3.67    0.52   2.79    4.80 1.00    2970    5321
```

Regression Coefficients:

```
      Estimate Est.Error 1-95%
Intercept          7.45    0.85   5.99    9.31 1.00    4031
dimer_rotlbfgs    -1.60    0.42  -2.45   -0.81 1.00    10344
rot_removalyes     0.65    0.49  -0.30    1.62 1.00    10602
dimer_rotlbfgs:rot_removalyes  0.06    0.60  -1.10    1.23 1.00    9521
Tail_ESS
Intercept          5602
dimer_rotlbfgs     9006
rot_removalyes     9400
dimer_rotlbfgs:rot_removalyes  8970
```

Draws were sampled using `sample(hmc)`. For each parameter, `Bulk_ESS` and `Tail_ESS` are effective sample size measures, and `Rhat` is the potential scale reduction factor on split chains (at convergence, `Rhat = 1`).

The full model reinforces the conclusions drawn from the simpler subset models. The main effect for the optimizer choice, `dimer_rotlbfgs`, is large, negative, and statistically discernible, with a coefficient of -1.60 (95% CI: [-2.45, -0.81]). In contrast, the main effect for `rot_removalyes` and the interaction term, `dimer_rotlbfgs:rot_removalyes`, are both small and have credible intervals that broadly overlap with zero.

This indicates that while the choice of optimizer has a significant impact on the reliability of the calculation, the decision to use rotation removal does not. Furthermore, the lack of a discernible interaction effect means that the performance penalty of using L-BFGS is consistent (though slightly higher reliability with rotation removal is indicated), regardless of the rotation removal setting. As before, all tested configurations show a very high absolute success rate (>99%).

Model diagnostics were excellent. All `Rhat` values are close to 1.0, and `Bulk_ESS` and `Tail_ESS` values are large, indicating good chain convergence. Trace plots (Figure 28) confirmed good mixing of the chains.

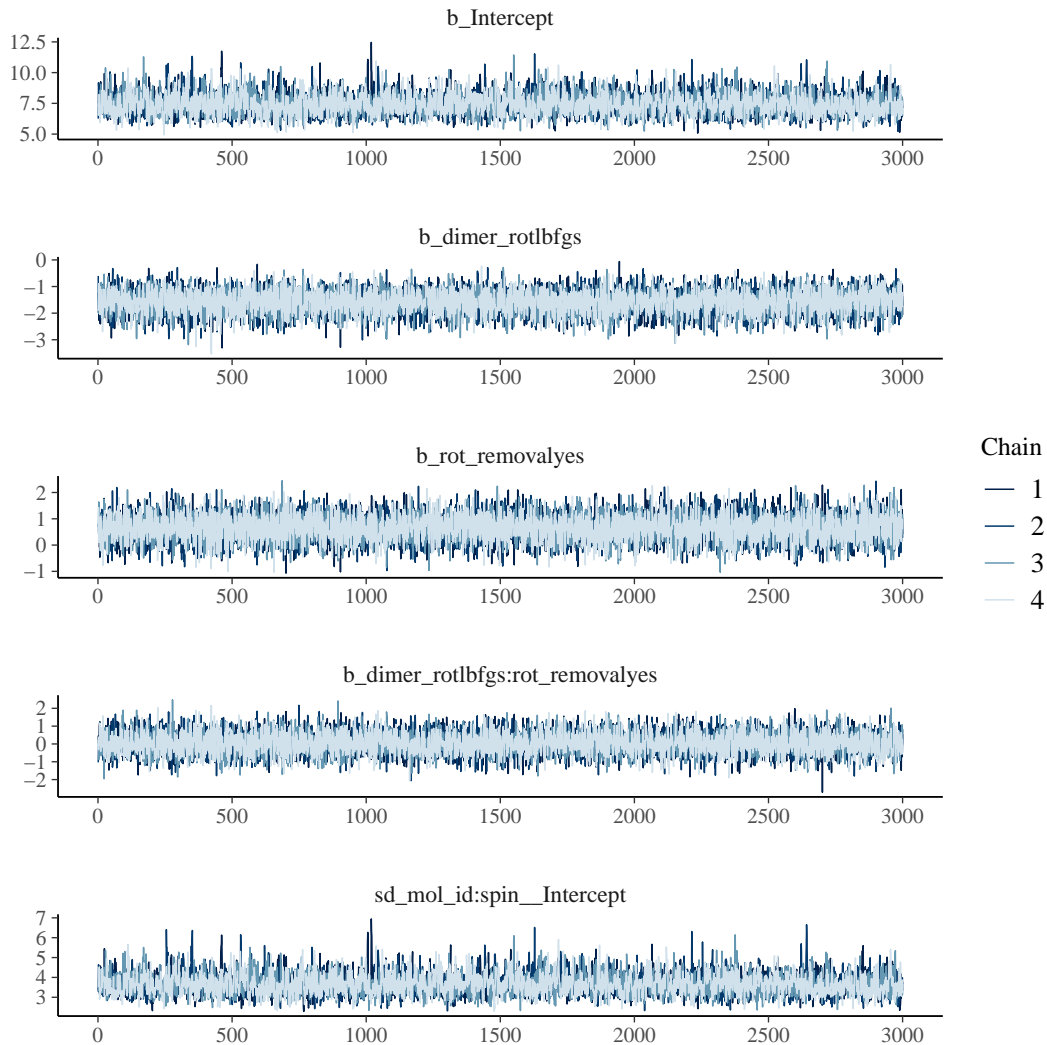


Figure 28: Trace plots for the main parameters of the combined success model, showing well-mixed chains.

Posterior predictive checks (Figure 29) indicate a good model fit, with the posterior predictive distribution closely matching the observed distribution of success.

Further diagnostics using the DHARMA package (Figure 30) also support the validity of the model, with residuals behaving as expected and showing no significant patterns or deviations from uniformity.

The practical effects are summarized in Table 7. The Odds Ratio for using L-BFGS versus CG is 0.20, a substantial and discernible reduction in the odds of success. The odds ratios for rotation removal and the interaction term both have wide credible intervals that contain 1.0, confirming they are not statistically discernible.

A subtle question is whether rotation removal has a benefit specifically for the L-BFGS optimizer. The model's median estimate for this conditional effect (the sum of the rot_removalyes and interaction effects) suggests that enabling rotation removal doubles the odds of success for L-BFGS. However, due to the high uncertainty in both of these parameters, this combined effect is also not statistically discernible and we cannot confidently claim it is a reliable improvement.

The combined success model provides robust, comprehensive evidence for a clear conclusion. For maximum reliability, the Conjugate Gradient (CG) optimizer should be used. The choice of enabling or disabling external rotation removal has no statistically discernible impact on the success rate. The optimal and most robust method is therefore CG, with or without rotation removal.

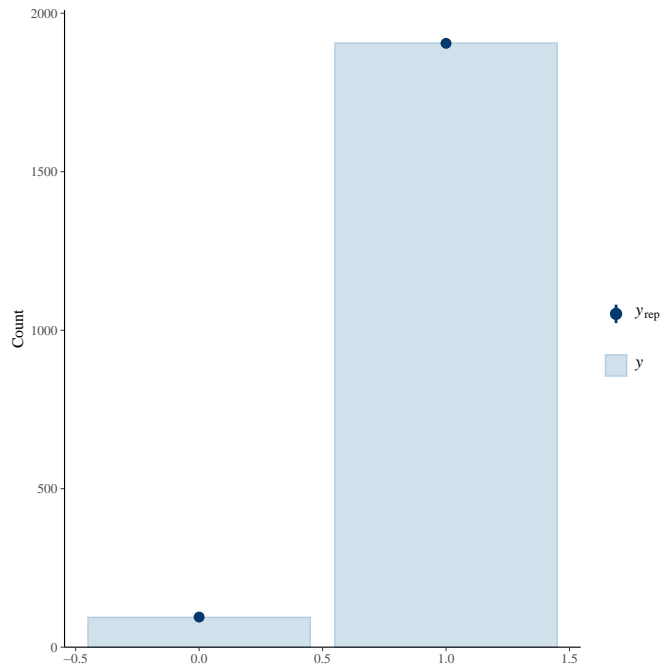


Figure 29: Posterior predictive check for the combined success model.

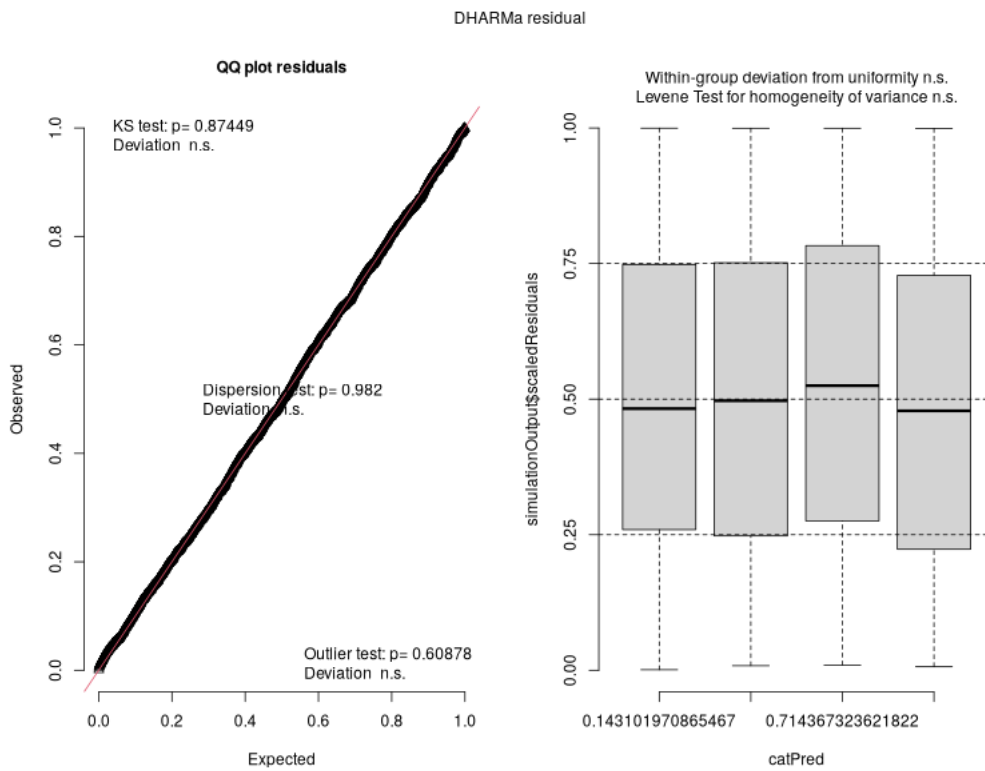


Figure 30: DHARMA diagnostic plots for the combined success model, showing a good fit with no significant deviations in residuals.

Table 7: Combined success model effects, including credible intervals.

Effect Type	Median Effect	95% CrI
Probability (CG Success)	1.0	[1.00, 1.00]
Odds Ratio (L-BFGS vs. CG)	0.2	[0.09, 0.45]
Interaction Odds Ratio	1.1	[0.33, 3.42]
Odds Ratio RotRemove (Yes vs. No)	1.9	[0.74, 5.07]
sd(Intercept) [molid:spin]	3.6	[2.79, 4.80]

References

- [1] APRÀ, E., BYLASKA, E. J., DE JONG, W. A., GOVIND, N., KOWALSKI, K., STRAATSMA, T. P., VALIEV, M., VAN DAM, H. J. J., ALEXEEV, Y., ANCHELL, J., ANISIMOV, V., AQUINO, F. W., ATTA-FYNN, R., AUTSCHBACH, J., BAUMAN, N. P., BECCA, J. C., BERNHOLDT, D. E., BHASKARAN-NAIR, K., BOGATKO, S., BOROWSKI, P., BOSCHEN, J., BRABEC, J., BRUNER, A., CAUËT, E., CHEN, Y., CHUEV, G. N., CRAMER, C. J., DAILY, J., DEEGAN, M. J. O., DUNNING, T. H., DUPUIS, M., DYALL, K. G., FANN, G. I., FISCHER, S. A., FONARI, A., FRÜCHTL, H., GAGLIARDI, L., GARZA, J., GAWANDE, N., GHOSH, S., GLAESEMANN, K., GÖTZ, A. W., HAMMOND, J., HELMS, V., HERMES, E. D., HIRAO, K., HIRATA, S., JACQUELIN, M., JENSEN, L., JOHNSON, B. G., JÓNSSON, H., KENDALL, R. A., KLEMM, M., KOBAYASHI, R., KONKOV, V., KRISHNAMOORTHY, S., KRISHNAN, M., LIN, Z., LINS, R. D., LITTLEFIELD, R. J., LOGSDAIL, A. J., LOPATA, K., MA, W., MARENICH, A. V., MARTIN DEL CAMPO, J., MEJIA-RODRIGUEZ, D., MOORE, J. E., MULLIN, J. M., NAKAJIMA, T., NASCIMENTO, D. R., NICHOLS, J. A., NICHOLS, P. J., NIEPLOCHA, J., OTERO-DE-LA-ROZA, A., PALMER, B., PANYALA, A., PIROJSIRIKUL, T., PENG, B., PEVERATI, R., PITNER, J., POLLACK, L., RICHARD, R. M., SADAYAPPAN, P., SCHATZ, G. C., SHELTON, W. A., SILVERSTEIN, D. W., SMITH, D. M. A., SOARES, T. A., SONG, D., SWART, M., TAYLOR, H. L., THOMAS, G. S., TIPPARAJU, V., TRUHLAR, D. G., TSEMEKHMANN, K., VAN VOORHIS, T., VÁZQUEZ-MAYAGOITIA, Á., VERMA, P., VILLA, O., VISHNU, A., VOGIATZIS, K. D., WANG, D., WEARE, J. H., WILLIAMSON, M. J., WINDUS, T. L., WOLIŃSKI, K., WONG, A. T., WU, Q., YANG, C., YU, Q., ZACHARIAS, M., ZHANG, Z., ZHAO, Y., AND HARRISON, R. J. NWChem: Past, present, and future. *Journal of Chemical Physics* 152, 18 (May 2020), 184102.
- [2] BAKER, J., AND CHAN, F. The location of transition states: A comparison of Cartesian, Z-matrix, and natural internal coordinates. *Journal of Computational Chemistry* 17, 7 (1996), 888–904.
- [3] BERAHAS, A. S., CURTIS, F. E., AND ZHOU, B. Limited-memory BFGS with displacement aggregation. *Mathematical Programming* 194, 1 (July 2022), 121–157.
- [4] BÜRKNER, P.-C. Brms: An R Package for Bayesian Multilevel Models Using Stan. *Journal of Statistical Software* 80, 1 (Aug. 2017), 1–28.
- [5] CANCÈS, E., LEGOLL, F., MARINICA, M.-C., MINOUKADEH, K., AND WILLAIME, F. Some improvements of the activation-relaxation technique method for finding transition pathways on potential energy surfaces. *Journal of Chemical Physics* 130, 11 (Mar. 2009), 114711.
- [6] CARPENTER, B., GELMAN, A., HOFFMAN, M. D., LEE, D., GOODRICH, B., BETANCOURT, M., BRUBAKER, M., GUO, J., LI, P., AND RIDDELL, A. Stan: A Probabilistic Programming Language. *Journal of Statistical Software* 76, 1 (2017).
- [7] CERJAN, C. J., AND MILLER, W. H. On finding transition states. *The Journal of Chemical Physics* 75, 6 (Sept. 1981), 2800–2806.
- [8] CHILL, S. T., STEVENSON, J., RUEHLE, V., SHANG, C., XIAO, P., FARRELL, J. D., WALES, D. J., AND HENKELMAN, G. Benchmarks for Characterization of Minima, Transition States, and Pathways in Atomic, Molecular, and Condensed Matter Systems. *Journal of Chemical Theory and Computation* 10, 12 (Dec. 2014), 5476–5482.
- [9] CHILL, S. T., WELBORN, M., TERRELL, R., ZHANG, L., BERTHET, J.-C., PEDERSEN, A., JÓNSSON, H., AND HENKELMAN, G. EON: Software for long time simulations of atomic scale systems. *Modelling and Simulation in Materials Science and Engineering* 22, 5 (July 2014), 055002.
- [10] EYRING, H. The activated complex in chemical reactions. *Journal of Chemical Physics* 3, 2 (Feb. 1935), 107–115.
- [11] FLEMING, P. J., AND WALLACE, J. J. How not to lie with statistics: The correct way to summarize benchmark results. *Communications of the ACM* 29, 3 (Mar. 1986), 218–221.
- [12] FU, X., WU, Z., WANG, W., XIE, T., KETEN, S., GOMEZ-BOMBARELLI, R., AND JAAKKOLA, T. Forces are not Enough: Benchmark and Critical Evaluation for Machine Learning Force Fields with Molecular Simulations, Oct. 2022.

- [13] GOSWAMI, R. Wailord: Parsers and Reproducibility for Quantum Chemistry. *Proceedings of the 21st Python in Science Conference* (2022), 193–197.
- [14] GOSWAMI, R. Dataset for Bayesian hierarchical models for quantitative estimates for performance metrics applied to saddle search algorithms, May 2025.
- [15] GOSWAMI, R., MASTEROV, M., KAMATH, S., PEÑA-TORRES, A., AND JÓNSSON, H. Efficient implementation of gaussian process regression accelerated saddle point searches with application to molecular reactions, May 2025.
- [16] GOSWAMI, R., MASTEROV, M., KAMATH, S., PEÑA-TORRES, A., AND JÓNSSON, H. Efficient Implementation of Gaussian Process Regression Accelerated Saddle Point Searches with Application to Molecular Reactions. *Journal of Chemical Theory and Computation* (July 2025).
- [17] GOSWAMI, R., AND S., R. High Throughput Reproducible Literate Phylogenetic Analysis. In *2022 Seventh International Conference on Parallel, Distributed and Grid Computing (PDGC)* (Nov. 2022), pp. 337–340.
- [18] GOSWAMI, R., S., R., GOSWAMI, A., GOSWAMI, S., AND GOSWAMI, D. Reproducible High Performance Computing without Redundancy with Nix. In *2022 Seventh International Conference on Parallel, Distributed and Grid Computing (PDGC)* (Nov. 2022), pp. 238–242.
- [19] GUNDE, M., JAY, A., POBERŽNIK, M., SALLES, N., RICHARD, N., LANDA, G., MOUSSEAU, N., MARTIN-SAMOS, L., AND HEMERYCK, A. Exploring potential energy surfaces to reach saddle points above convex regions. *The Journal of Chemical Physics* 160, 23 (June 2024), 232501.
- [20] HENKELMAN, G., AND JÓNSSON, H. A dimer method for finding saddle points on high dimensional potential surfaces using only first derivatives. *The Journal of Chemical Physics* 111, 15 (Oct. 1999), 7010–7022.
- [21] HERMES, E. D., SARGSYAN, K., NAJM, H. N., AND ZÁDOR, J. Sella, an Open-Source Automation-Friendly Molecular Saddle Point Optimizer. *Journal of Chemical Theory and Computation* 18, 11 (Nov. 2022), 6974–6988.
- [22] HEYDEN, A., BELL, A. T., AND KEIL, F. J. Efficient methods for finding transition states in chemical reactions: Comparison of improved dimer method and partitioned rational function optimization method. *The Journal of Chemical Physics* 123, 22 (Dec. 2005), 224101.
- [23] HOMAN, M. D., AND GELMAN, A. The No-U-turn sampler: Adaptively setting path lengths in Hamiltonian Monte Carlo. *The Journal of Machine Learning Research* 15, 1 (Jan. 2014), 1593–1623.
- [24] HUBER, S. P. Automated reproducible workflows and data provenance with AiiDA. *Nature Reviews Physics* 4, 7 (July 2022), 431–431.
- [25] JENSEN, F. *Introduction to Computational Chemistry*, third edition ed. Wiley, Chichester, UK ; Hoboken, NJ, 2017.
- [26] KÄSTNER, J., AND SHERWOOD, P. Superlinearly converging dimer method for transition state search. *The Journal of Chemical Physics* 128, 1 (Jan. 2008), 014106.
- [27] KOISTINEN, O.-P., ÁSGEIRSSON, V., VEHTARI, A., AND JÓNSSON, H. Minimum Mode Saddle Point Searches Using Gaussian Process Regression with Inverse-Distance Covariance Function. *Journal of Chemical Theory and Computation* 16, 1 (Jan. 2020), 499–509.
- [28] KRIEGEL, H.-P., SCHUBERT, E., AND ZIMEK, A. The (black) art of runtime evaluation: Are we comparing algorithms or implementations? *Knowledge and Information Systems* 52, 2 (Aug. 2017), 341–378.
- [29] KUFFNER, T. A., AND WALKER, S. G. Why are p-Values Controversial? *The American Statistician* 73, 1 (Jan. 2019), 1–3.
- [30] LENG, J., GAO, W., SHANG, C., AND LIU, Z.-P. Efficient softest mode finding in transition states calculations. *Journal of Chemical Physics* 138, 9 (Mar. 2013), 94110.
- [31] MCELREATH, R. *Statistical Rethinking: A Bayesian Course with Examples in R and Stan*, 2 ed. CRC Texts in Statistical Science. Taylor and Francis, CRC Press, Boca Raton, 2020.
- [32] MCSHANE, B. B., GAL, D., GELMAN, A., ROBERT, C., AND TACKETT, J. L. Abandon Statistical Significance. *The American Statistician* 73, sup1 (Mar. 2019), 235–245.
- [33] MELANDER, M., LAASONEN, K., AND JÓNSSON, H. Removing External Degrees of Freedom from Transition-State Search Methods using Quaternions. *Journal of Chemical Theory and Computation* 11, 3 (Mar. 2015), 1055–1062.
- [34] MÖLDER, F., JABLONSKI, K. P., LETCHER, B., HALL, M. B., TOMKINS-TINCH, C. H., SOCHAT, V., FORSTER, J., LEE, S., TWARDZIOK, S. O., KANITZ, A., WILM, A., HOLTGREWE, M., RAHMANN, S., NAHNSEN, S., AND KÖSTER, J. Sustainable data analysis with Snakemake, Apr. 2021.

- [35] MOUSSEAU, N., AND BARKEMA, G. T. Traveling through potential energy landscapes of disordered materials: The activation-relaxation technique. *Physical Review E* 57, 2 (Feb. 1998), 2419–2424.
- [36] MOUSSEAU, N., BÉLAND, L. K., BROMMER, P., JOLY, J.-F., EL-MELLOUHI, F., MACHADO-CHARRY, E., MARINICA, M.-C., AND POCHET, P. The Activation-Relaxation Technique: ART Nouveau and Kinetic ART. *Journal of Atomic and Molecular Physics* 2012, 1 (2012), 925278.
- [37] MUNRO, L. J., AND WALES, D. J. Defect migration in crystalline silicon. *Physical Review B* 59, 6 (Feb. 1999), 3969–3980.
- [38] NICHOLS, J., TAYLOR, H., SCHMIDT, P., AND SIMONS, J. Walking on potential energy surfaces. *Journal of Chemical Physics* 92, 1 (Jan. 1990), 340–346.
- [39] NOCEDAL, J., AND WRIGHT, S. J. *Numerical Optimization*, 2nd ed ed. Springer Series in Operations Research. Springer, New York, 2006.
- [40] O’HARA, R. B., AND KOTZE, D. J. Do not log-transform count data. *Methods in Ecology and Evolution* 1, 2 (2010), 118–122.
- [41] OLSEN, R. A., KROES, G. J., HENKELMAN, G., ARNALDSSON, A., AND JÓNSSON, H. Comparison of methods for finding saddle points without knowledge of the final states. *The Journal of Chemical Physics* 121, 20 (Nov. 2004), 9776–9792.
- [42] PECHUKAS, P. Recent developments in transition state theory. *Berichte der Bunsen-Gesellschaft für Physikalische Chemie* 86, 5 (1982), 372–378.
- [43] POBERZNIK, M., GUNDE, M., SALLES, N., JAY, A., HEMERYCK, A., RICHARD, N., MOUSSEAU, N., AND MARTIN-SAMOS, L. pARTn: A plugin implementation of the Activation Relaxation Technique nouveau that takes over the FIRE minimisation algorithm. *Computer Physics Communications* 295 (Feb. 2024), 108961.
- [44] SALLERMANN, M., GOSWAMI, A., PEÑA-TORRES, A., AND GOSWAMI, R. Flowy: High performance probabilistic lava emplacement prediction, June 2024.
- [45] STARK, W. G., VAN DER OORD, C., BATATIA, I., ZHANG, Y., JIANG, B., CSÁNYI, G., AND MAURER, R. J. Benchmarking of machine learning interatomic potentials for reactive hydrogen dynamics at metal surfaces, Mar. 2024.
- [46] TALIRZ, L., KUMBHAR, S., PASSARO, E., YAKUTOVICH, A. V., GRANATA, V., GARGIULO, F., BORELLI, M., UHRIN, M., HUBER, S. P., ZOUPANOS, S., ADORF, C. S., ANDERSEN, C. W., SCHÜTT, O., PIGNEDOLI, C. A., PASSERONE, D., VANDEVONDELE, J., SCHULTHESS, T. C., SMIT, B., PIZZI, G., AND MARZARI, N. Materials cloud, a platform for open computational science. *Scientific Data* 7, 1 (Sept. 2020), 299.
- [47] WALES, D. J., DOYE, J. P. K., MILLER, M. A., MORTENSON, P. N., AND WALSH, T. R. Energy landscapes: From clusters to biomolecules. In *Advances in Chemical Physics*. John Wiley & Sons, Ltd, 2000, pp. 1–111.
- [48] ZENG, Y., XIAO, P., AND HENKELMAN, G. Unification of algorithms for minimum mode optimization. *The Journal of Chemical Physics* 140, 4 (Jan. 2014), 044115.